JGR Oceans

RESEARCH ARTICLE
10.1029/2023JC020303

Radium Isotopes as Tracers of Shelf-Basin Exchange Processes in the Eastern Arctic Ocean

Lauren Kipp[1], Matthew Charette[2], Alyssa Robbins[1], Andrey Pnyushkov[3], Igor Polyakov[3], and Laura Whitmore[3]

[1]Department of Environmental Science, Rowan University, Glassboro, NJ, USA, [2]Department of Marine Chemistry & Geochemistry, Woods Hole Oceanographic Institution, Woods Hole, MA, USA, [3]International Arctic Research Center, University of Alaska Fairbanks, Fairbanks, AK, USA

Key Points:

- In 2021, shelf- and river-influenced waters crossed the shelf-basin boundary near 170°E, indicating the likely position of the Transpolar Drift origin
- Models suggest a residence time of ~13 months in the Laptev and East Siberian Seas before surface water enters the central Arctic Ocean
- The Laptev, East Siberian, and Chukchi Shelves contribute a disproportionately high amount of radium to Arctic surface waters

Correspondence to:
L. Kipp,
kipp@rowan.edu

Citation:
Kipp, L., Charette, M., Robbins, A., Pnyushkov, A., Polyakov, I., & Whitmore, L. (2023). Radium isotopes as tracers of shelf-basin exchange processes in the Eastern Arctic Ocean. *Journal of Geophysical Research: Oceans*, *128*, e2023JC020303. https://doi.org/10.1029/2023JC020303

Received 31 JUL 2023
Accepted 15 NOV 2023

Abstract Radium isotopes, which are sourced from sediments, are useful tools for studying potential climate-driven changes in the transfer of shelf-derived elements to the open Arctic Ocean. Here we present observations of radium-228 and radium-226 from the Siberian Arctic, focusing on the shelf-basin boundary north of the Laptev and East Siberian Seas. Water isotopes and nutrients are used to deconvolve the contributions from different water masses in the study region, and modeled currents and water parcel back-trajectories provide insights on water pathways and residence times. High radium levels and fractions of meteoric water, along with modeled water parcel back-trajectories, indicate that shelf- and river-influenced water left the East Siberian Shelf around 170°E in 2021; this is likely where the Transpolar Drift was entering the central Arctic. A transect extending from the East Siberian Slope into the basin is used to estimate a radium-228 flux of 2.67×10^7 atoms m^{-2} d^{-1} (possible range of 1.23×10^7–1.04×10^8 atoms m^{-2} d^{-1}) from slope sediments, which is comparable to slope fluxes in other regions of the world. A box model is used to determine that the flux of radium-228 from the Laptev and East Siberian Shelves is 9.03×10^7 atoms m^{-2} d^{-1} (possible range of 3.87×10^7–1.56×10^8 atoms m^{-2} d^{-1}), similar to previously estimated fluxes from the Chukchi Shelf. These three shelves contribute a disproportionately high amount of radium to the Arctic, highlighting their importance in regulating the chemistry of Arctic surface waters.

Plain Language Summary Half of the Arctic Ocean is composed of shallow seas that extend over the continental shelf, so understanding what controls the chemical composition of the seawater in these regions is imperative to predicting how the Arctic Ocean as a whole may respond to climate change. Radium isotopes are naturally occurring radioactive elements that are produced in seafloor sediments, and they can be used to study the transfer of elements from the continental shelf into the overlying water. Here we combine measurements of radium isotopes with other chemical tracers and physical oceanographic models to study the transport and chemical signature of the Laptev and East Siberian Seas into the open Arctic Ocean. We find that the transport of elements from shelf sediments into the ocean is particularly strong in these seas and in the neighboring Chukchi Sea. Our data indicates that this region has an impact on the chemistry of the broader Arctic Ocean and emphasizes the need to continue to monitor this area for potential climate-driven changes.

1. Introduction

The Arctic Ocean is unique from other ocean basins due to its strong terrestrial influences: large, shallow continental shelves comprise over half of the basin area (Jakobsson, 2002) and it receives ~10% of global river discharge despite containing only ~1% of the global ocean volume (Aagaard & Carmack, 1989; McClelland et al., 2012). Sediment-water exchange over the shelf and river discharge therefore act as important sources and sinks for elements to Arctic surface waters, including those that are biologically utilized such as carbon, nutrients, and trace metals (Anderson et al., 2017; Brown et al., 2016; Charette et al., 2020; Jensen et al., 2019; Klunder et al., 2012; Nakayama et al., 2011; Vieira et al., 2018; Wheeler et al., 1997).

The Arctic is warming up to four times faster than the global average (since 1970; Chylek et al., 2022; Rantanen et al., 2022), and climate-driven changes are impacting the transfer of elements into Arctic seas. River discharge is increasing (Peterson et al., 2002; Rawlins et al., 2010), and rising air and sea temperatures are driving increased coastal erosion (Günther et al., 2013) and permafrost thaw (Luo et al., 2016). The loss of sea ice over the shallow shelf seas allows enhanced wind-driven mixing and turbulence (Polyakov, Rippeth, Fer, Baumann, et al., 2020;

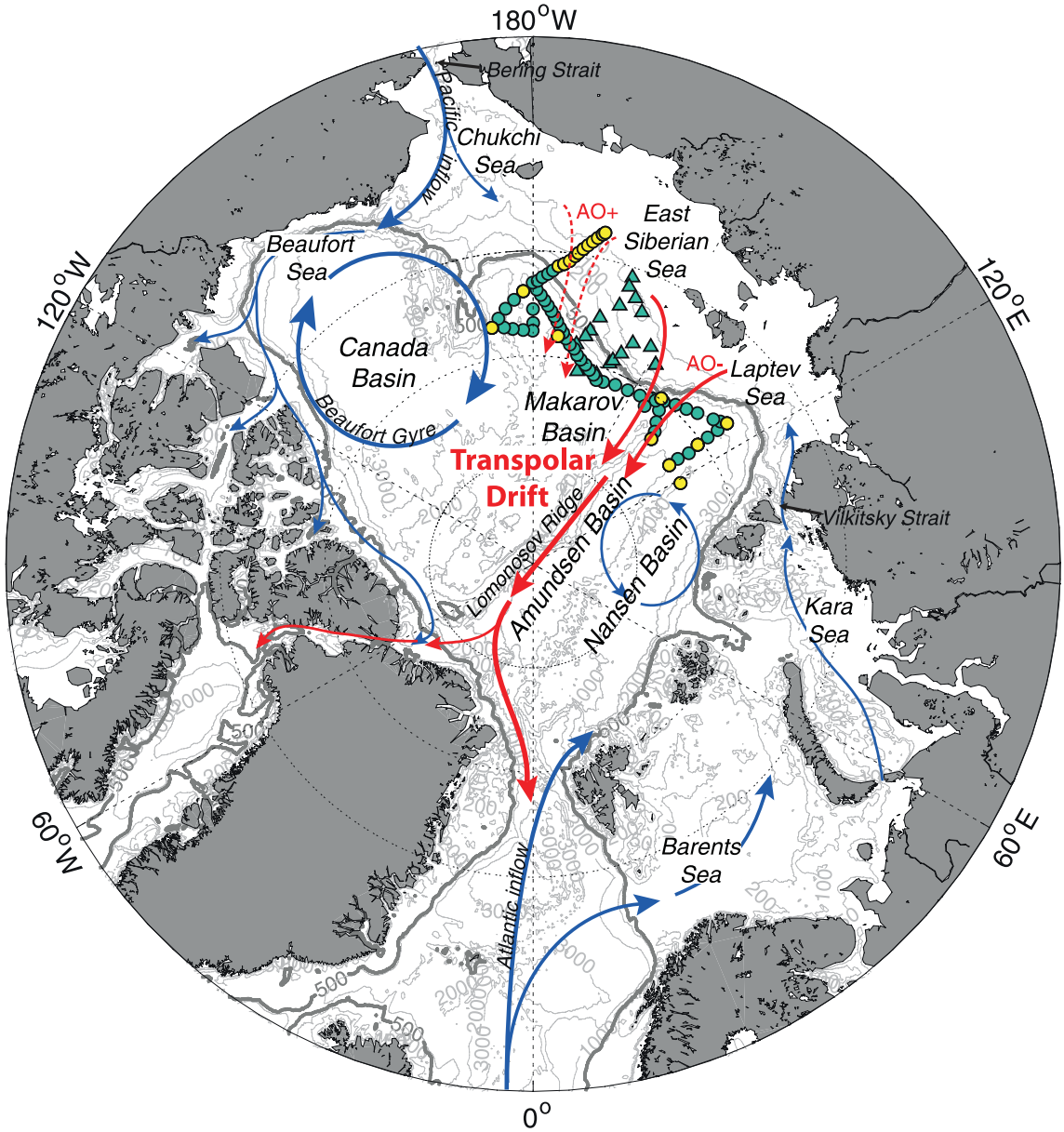

Figure 1. Map of the Arctic Ocean with the approximate pathway of the Transpolar Drift (TPD) (red arrows) and other notable surface circulation pathways (blue arrows). The origin of the TPD under positive and negative Arctic Oscillation states is shown with dashed and solid arrows, respectively. Colored symbols indicate the location of surface (teal) and sub-surface (yellow) sampling in 2021 (circles) and 2018 (triangles). The 500 m isobath is shown in bold.

Rainville & Woodgate, 2009; Schulz et al., 2021), which can facilitate transport of elements from the benthic boundary layer into the overlying water column (Kipp et al., 2018; Schulz et al., 2022).

While these changes extend from the nearshore environment to the continental slope, shifts in shelf sea chemistry can be rapidly propagated across the Arctic basin via the Transpolar Drift (TPD), a surface current that originates north of Russia in the Laptev and East Siberian Seas (Figure 1). The TPD carries river- and shelf-influenced waters across the Arctic, serving as an important pathway for nutrient, carbon, and trace metal delivery to the central basin (Charette et al., 2020; Kadko et al., 2019; Letscher et al., 2011; Wheeler et al., 1997). Recent evidence suggests that the chemistry of the TPD may be changing as a result of increased fluxes of shelf-derived elements, likely driven by the heightened turbulence in the shallow and increasingly ice-free shelf seas where the TPD originates (Kipp et al., 2018; Rutgers van der Loeff et al., 2018). Combined with changing light limitations arising from a reduction in sea ice cover (Ardyna et al., 2014; Arrigo et al., 2008), this shift in surface water

chemistry has the potential to impact primary production across the Arctic. However, observations of these chemical changes have generally poor temporal resolution and improved monitoring of the biogeochemical changes in the Arctic shelf seas and TPD is needed to improve our understanding of the impacts of climate change on the Arctic.

The quartet of radium isotopes (^{223}Ra, $t_{1/2}$ = 11.4 days; ^{224}Ra, $t_{1/2}$ = 3.66 days; ^{228}Ra, $t_{1/2}$ = 5.75 years; ^{226}Ra, $t_{1/2}$ = 1,600 years) are continuously produced through the radioactive decay of thorium and uranium in sediments and are relatively soluble in seawater. Elevated concentrations of Ra isotopes in marine systems therefore indicate significant interaction between seawater and sediment at ocean boundaries, via processes such as diffusive porewater exchange, river or submarine groundwater discharge, or desorption from eroded coastal sediments (Burt et al., 2013; Dulaiova et al., 2006; Kelly & Moran, 2002; Moore & Todd, 1993; Peterson et al., 2008; Reid, 1984; Rodellas et al., 2017). Radium isotopes can also be used to quantify fluxes of elements that have the same margin sources, such as trace metals (Sanial et al., 2018; Vieira et al., 2018) and nutrients (Moody, 2022; Moore, 2006).

The half-life of ^{228}Ra makes this isotope a particularly useful tracer in the Arctic, as it responds to changes in sediment-water exchange processes on timescales relevant to anthropogenic climate change (~years) and does not significantly decay or exhibit removal onto particles on the timescale of transport from the shelf to the basin (Moore & Dymond, 1991; van Beek et al., 2007). The ratio of ^{228}Ra/^{226}Ra is also a useful diagnostic tool because Ra fluxes from shelf sediments have a higher ratio than those derived from rivers (Rutgers van der Loeff et al., 2003).

The Arctic Radium Isotope Observing Network (ARION) aims to elucidate the seasonal and interannual variability in ^{228}Ra signals transported from the eastern Arctic shelves to the central basin to evaluate the use of this isotope as a tracer of climate-driven changes in Arctic Ocean chemistry (Kipp & Charette, 2022). Water sampling along the slopes of the Laptev and East Siberian Seas is used to construct a long term record of the radium activities leaving these shelves, which serve as the origin point for the TPD. Here we present ^{228}Ra and ^{226}Ra activities measured on the first ARION water column sampling expedition in fall 2021 and compare these results to samples collected in the ESS in 2018 and to previously published data collected from the TPD and the Chukchi Sea.

2. Methods

2.1. 2018 Sample Collection

Surface water samples (60L) were collected from the ESS and Slope between 21 August and 24 September 2018 during the Nansen and Amundsen Basin Observational System (NABOS) expedition on the *R/V Akademik Tryoshnikov*. Water was collected from 6.5 m using the ship's underway sampling system and stored in plastic cubitainers. After the cruise, samples were shipped back to the Woods Hole Oceanographic Institution (WHOI) for processing.

The water samples were sub-sampled for water isotopes (2 mL) and salinity (100 mL), then filtered at <1 L/min through acrylic fiber coated in manganese oxide (MnO_2), which scavenges Ra (Moore & Reid, 1973). A plug of untreated acrylic fiber was included to remove any coarse suspended sediments. After filtration, fibers were rinsed with Ra-free deionized water to remove any remaining particles and salts. Evaporation during storage between sample collection and processing may have impacted salinity and water isotope samples; however, a comparison to bottle samples collected from 10 m on the conductivity-temperature-depth (CTD) rosette (Bolt, 2021) shows only small average offsets for $\delta^{18}O$ (0.35‰) and salinity (0.08).

2.2. 2021 Sample Collection

Radium, water isotope, and salinity samples were collected along the Laptev and ESS slopes, the northern ESS, and in the Amundsen and Makarov Basins during the NABOS expedition on the *R/V Akademik Tryoshnikov* from 10 September to 19 October 2021 (Figure 1).

Surface samples (120–130 L) were collected from 1 to 2 m using a submersible pump (Tsurumi 50TM2.75) lowered by hand. The CTD rosette was used to acquire samples from additional depths; six 10-L Niskin bottles were tripped at the same depth and combined into one 60L sample. Depth profiles down to 250 m were collected at four depths (20, 40, 100, 250 m) and near-bottom samples were collected when possible over the East Siberian

Shelf and Slope. Subsamples for water isotopes (2 mL) and salinity (100 mL) were collected from the plastic drums holding the 120- or 60-L radium samples. Water isotope samples were stored in glass vials with no headspace and kept refrigerated until analysis.

Radium samples were filtered through untreated acrylic fiber to remove suspended sediments, and then through ~10–15 g of MnO_2-coated acrylic fiber to scavenge Ra (Moore & Reid, 1973). Fibers were packed into PVC housings 1″ or 1.5″ inches in diameter. Flow rates were kept below 1 L min^{-1}. After filtration, fibers were rinsed with Ra-free deionized water to remove any remaining particles and salts.

Extraction efficiency was checked by filtering a subset of samples through two fibers in series (denoted "A" and "B" fibers) and is reported as "breakthrough", or the amount of ^{228}Ra or ^{226}Ra on the B fiber relative to the A fiber, as a percentage. The Ra activities on the B fibers varied based on the size of housing and amount of fiber used in the A filter. In all cases the B fiber consisted of 10 g of MnO_2 fiber in a 1" housing. Breakthrough for ^{228}Ra and ^{226}Ra was higher when the A fiber had only 10 g (7.2% and 5.3%, respectively) versus 15g in a 1.5" housing (5.8% and 3.2%, respectively). The most common collection method for 120L samples was 15 g of fiber in a 1.5" housing. The 60 L samples were always collected onto 10 g of fiber in a 1" housing. Breakthrough was lowest in this scenario; the ^{228}Ra measured on the B fiber was only 0.6% of that measured on the A fiber, and the ^{226}Ra on the B fiber was below detection. As a result of these differences in the extraction of Ra onto the MnO_2 fiber, some of the Ra activities may be slightly underestimated, but the percentage of Ra loss is similar to the reported error values (typically ~2–7% for ^{228}Ra, ~1–3% for ^{226}Ra).

An intercalibration between the surface and CTD sampling was performed at a test station before Station 1; two 60L samples were collected from the CTD rosette and one 130 L sample was collected using the submersible pump. The ^{228}Ra activities measured on the two small volume samples were within error of that measured on the larger volume sample (3.74 ± 0.55 dpm/100 L, 3.81 ± 0.48 dpm/100 L, and 3.16 ± 0.39 dpm/100 L, respectively), while the ^{226}Ra activities were slightly higher in the small volume samples compared to the large volume sample (7.51 ± 0.26 dpm/100 L, 7.53 ± 0.32 dpm/100 L, and 6.44 ± 0.18 dpm/100 L, respectively). The differences between the large and small volume samples may be due in part to the different cartridges used during filtration. The CTD rosette may also have captured slightly deeper water compared to the surface pump (~5 m compared to 1–2 m), though the radium activities are likely to be well-mixed throughout the surface layer.

Although the sample processing for the 2018 samples took place on shore rather than immediately following sample collection, the same approach was used in both years (filtration at <1 L min^{-1} through MnO_2 fiber) so there are no methodological differences that should affect the comparison between these two data sets. The time elapsed between sample collection and processing in 2018 (3 months) resulted in a negligible amount of ^{228}Ra decay (~3%).

2.3. Sample Analysis

On shore, fibers were ashed in a muffle furnace at 820°C for 12 hr. Ash was subsequently packed into polystyrene test tubes and sealed with epoxy to prevent radon loss. After waiting at least three weeks for daughter isotopes to reach equilibrium, ^{228}Ra and ^{226}Ra were measured using gamma spectroscopy. All of the samples collected in 2018 were analyzed using well-type germanium gamma detectors located at WHOI. For the 2021 expedition, samples were divided between a 16 mm well-type small anode 200 cc germanium crystal (SAGe) gamma detector located at Rowan University and two traditional 16 mm well-type 190 cc germanium crystal detectors located at WHOI. A subset of samples and reference materials were analyzed at both Rowan and WHOI to ensure intercalibration between the two labs. Radium-228 was reported as an average of the lines for ^{228}Ac (338 and 911 keV) while ^{226}Ra was based on the line for ^{214}Pb (352 keV). Detector efficiencies were determined using a set of reference materials made of ashed Mn-fiber spiked with ^{226}Ra (NIST standard reference material (SRM) #4967A) and ^{232}Th (sourced from thorium nitrate powder) with daughters in equilibrium and prepared the same way as the samples. Blank ash (ashed MnO_2 fiber that has not been in contact with any seawater) was analyzed in the same way as the samples, and any measurable ^{228}Ra and ^{226}Ra activities were subtracted from the sample activities. There were measurable blanks for the 338, 352, and 911 keV lines on the SAGe detector, and for the 352 keV line on both traditional well detectors; the average blank corrections for the 338, 352, and 911 keV lines were 7.3%, 9.1%, and 5.7%, respectively, of the total counts per minute in the sample.

Water isotopes ($\delta^{18}O$ and $\delta^{2}H$) were analyzed by the Stable Isotope Facility at the University of Wyoming using Cavity Ring Down Spectroscopy on a Picarro L2130-I liquid water analyzer and are reported in permil (‰) with respect to Vienna Standard Mean Ocean Water. Uncertainties calculated based on repeated (n = 12) measurements of three SRMs were <0.15‰ for the 2018 samples and <0.3‰ for the 2021 samples. Salinity samples were measured at WHOI using a Guildline Autosal calibrated with International Association for Physical Sciences of the Ocean standard seawater. This instrument has an accuracy of ±0.003 and a resolution of 0.0002 at salinity 35. In cases where a salinity sample was not collected in coordination with the radium sample (n = 19), the salinity was assumed to be the same as that measured on CTD rosette samples collected within 5 m of the Ra sample. The average offset between salinity samples measured at WHOI and the salinity measured via the CTD was −0.09 (offset ranged from −0.79 to +0.29).

2.4. Water Mass Fraction Calculations

Assuming that the four main water masses present in the Arctic Ocean (Atlantic-derived seawater, Pacific-derived seawater, meteoric water, and sea ice meltwater) have distinct and consistent properties, the relative contributions of each water mass to a given sample can be determined using a system of linear equations. The conservative tracers $\delta^{18}O$ and salinity (S) are used to distinguish between the fractions of meteoric water (f_{MET}), sea ice meltwater (f_{SIM}), and seawater (f_{SW}) based on defined values for each endmember and the $\delta^{18}O$ and S measured in the sample ($\delta^{18}O_{obs}$ and S_{obs}, respectively), as described in Equations 1–3:

$$f_{MET} + f_{SIM} + f_{SW} = 1 \quad (1)$$

$$f_{MET} \bullet S_{MET} + f_{SIM} \bullet S_{SIM} + f_{SW} \bullet S_{SW} = S_{obs} \quad (2)$$

$$f_{MET} \bullet \delta^{18}O_{MET} + f_{SIM} \bullet \delta^{18}O_{SIM} + f_{SW} \bullet \delta^{18}O_{SW} = \delta^{18}O_{obs} \quad (3)$$

In the case of sea ice formation, f_{SIM} will be a negative value. To separate the contributions of Atlantic- and Pacific-derived seawater, a third tracer is needed. Because nutrient concentrations are high in Pacific inflow compared to Atlantic inflow, the ratio of either nitrate (NO_3^-) or total dissolved inorganic nitrogen (DIN = $NO_3^- + NO_2^- + NH_4$) to phosphate (PO_4^{-3}) (Arctic N:P ratio or ANP tracer) can be used as a quasi-conservative tracer (Jones et al., 1998; Newton et al., 2013; Yamamoto-Kawai et al., 2008). Uptake, regeneration, nitrification and denitrification over Arctic shelves can cause variation from traditional Redfield ratios (e.g., Alkire et al., 2015, 2019; Bauch et al., 2011; Devol et al., 1997), thus the N:P ratio of Atlantic and Pacific endmembers is typically defined based on observations. The relative amount of Atlantic- and Pacific-derived seawater can then be computed based on the distance from the Atlantic and Pacific lines on a plot of N:P, as described in Equations 4–6,

$$P_{ATL} = (N_{obs} + ATL_{int})/ATL_{slope} \quad (4)$$

$$P_{PAC} = (N_{obs} + PAC_{int})/PAC_{slope} \quad (5)$$

$$R_{PAC} = (P_{obs} - P_{ATL})/(P_{PAC} - P_{ATL}) \quad (6)$$

where P_{ATL} and P_{PAC} are the concentrations of phosphate predicted by the N:P relationship of the Atlantic and Pacific lines, respectively, ATL_{int} and ATL_{slope} are the intercept and slope of the Atlantic line, PAC_{int} and PAC_{slope} are the intercept and slope of the Pacific line, R_{PAC} is the fraction of the seawater endmember that is Pacific-derived, and N_{obs} and P_{obs} are the measured DIN and phosphate concentrations.

The fraction of Pacific-derived seawater is used to determine S_{SW} and $\delta^{18}O_{SW}$, following Equations 7 and 8 (Yamamoto-Kawai et al., 2008),

$$S_{SW} = S_{PAC} \bullet R_{PAC} + S_{ATL} \bullet (1 - R_{PAC}) \quad (7)$$

$$\delta^{18}O_{SW} = \delta^{18}O_{PAC} \bullet R_{PAC} + \delta^{18}O_{ATL} \bullet (1 - R_{PAC}) \quad (8)$$

where S_{PAC} and S_{ATL} are the salinity of Pacific- and Atlantic-derived seawater, respectively, and $\delta^{18}O_{PAC}$ and $\delta^{18}O_{ATL}$ are the $\delta^{18}O$ values of Pacific- and Atlantic-derived seawater, respectively. Once S_{SW} and $\delta^{18}O_{SW}$ are determined, these values are used in Equations 2 and 3 to calculate f_{MET}, f_{SIM}, and f_{SW}. The f_{SW} is then deconvolved

Table 1
Endmember Values Used to Determine Water Mass Fractions

Endmember	Salinity[a]	$\delta^{18}O$ (‰)[a]	Slope[b]	Intercept (μmol/kg)[b]
Meteoric water	0	−22 to −18	n/a	n/a
Sea ice meltwater	2–8	0–1	n/a	n/a
Atlantic-derived seawater	34.85–35.00	0.25–0.35	17–18.4	2–3.6
Pacific-derived seawater	32.0–32.7	−1.3 to −0.8	12.3–15.3	10.5–14.5

[a]Alkire et al., 2015. [b]Alkire et al., 2015; Jones et al., 2008, 1998; Newton et al., 2013; Whitmore et al., 2020; Yamamoto-Kawai et al., 2008.

into the fraction of Pacific- and Atlantic-derived seawater in the original sample (f_{PAC} and f_{ATL}, respectively) using Equations 9 and 10 (Yamamoto-Kawai et al., 2008):

$$f_{PAC} = f_{SW} \bullet R_{PAC} \quad (9)$$

$$f_{ATL} = f_{SW} \bullet (1 - R_{PAC}) \quad (10)$$

The Atlantic and Pacific N:P ratios can vary in time and space, and different studies have defined slightly different relationships. We have therefore applied a Monte Carlo approach to calculate the expected N:P ratios and R_{PAC}, based on the range in slopes and intercepts reported in the literature (Table 1) (Alkire et al., 2015; Jones et al., 1998, 2008; Newton et al., 2013; Whitmore et al., 2020; Yamamoto-Kawai et al., 2008). Similarly, a second Monte Carlo simulation was done to determine the endmember values for S and $\delta^{18}O$, using the approach and range of endmember values described in Alkire et al. (2015) (Table 1).

Although variation in chosen endmember values can cause notable differences in the resulting Atlantic- and Pacific-derived seawater fractions (e.g., Alkire et al., 2015 report a median standard deviation of 13% in the Pacific-derived seawater fractions), variability in the meteoric water and sea ice meltwater fractions is typically much less (e.g., ≤1%, Alkire et al., 2015). We compared the meteoric water fractions computed using the Monte Carlo-calculated N:P ratios to those calculated using discretely defined Atlantic and Pacific N:P lines to ensure that this did not significantly change our results; using the lines defined in Newton et al. (2013) and Whitmore et al. (2020) resulted in an average −0.13% offset from the Monte Carlo-derived fractions (maximum of −1.80%), and using the lines defined in Yamamoto-Kawai et al. (2008) resulted in an average −0.11% offset (maximum of −1.31%). The median standard deviation in f_{MET} calculated during the Monte Carlo simulation was 0.91%. Based on this, we assigned a conservative, upper limit error value of 2% to our meteoric water fractions. To enable a comparison to studies from other years, f_{MET} for all other studies included in our comparisons was re-calculated following the approach above.

2.5. Water Parcel Trajectory Calculations

In addition to water chemistry observations, we employed monthly velocities from the ORAS5 reanalysis system in the upper 10-m layer to calculate water parcel trajectories and estimate the residence time of surface waters on the Siberian shelf. The ORAS5 system is based on the three-dimensional Nucleus for European Modeling of the Ocean model, coupled with the thermodynamic-dynamic sea-ice model LIM2, and the NEMOVAR data assimilation system (for further details, see Zuo et al., 2019). The ORAS5 data set provides global coverage with an eddy-permitting horizontal resolution of 0.25° in the Arctic Ocean and 75 vertical z-levels. The model was driven by the atmospheric reanalysis ERA-Interim from the European Centre for Medium-range Weather Forecasts (Dee et al., 2011).

We conducted simulations of parcel trajectories for three distinct periods: 2012–2015, 2015–2018, and 2018–2021, which cover the duration of radium observations used in this study. Following the methodology described by Polyakov et al. (2023), for each period, we released 20 tracers evenly distributed along the section crossing the origin of the TPD at the Siberian continental slope. Trajectories were computed for 3 years backward in time, which was sufficient for the tracers to reach the coasts of the East Siberian, Laptev, and Kara Seas, or to exit the Arctic Ocean through the Bering Strait.

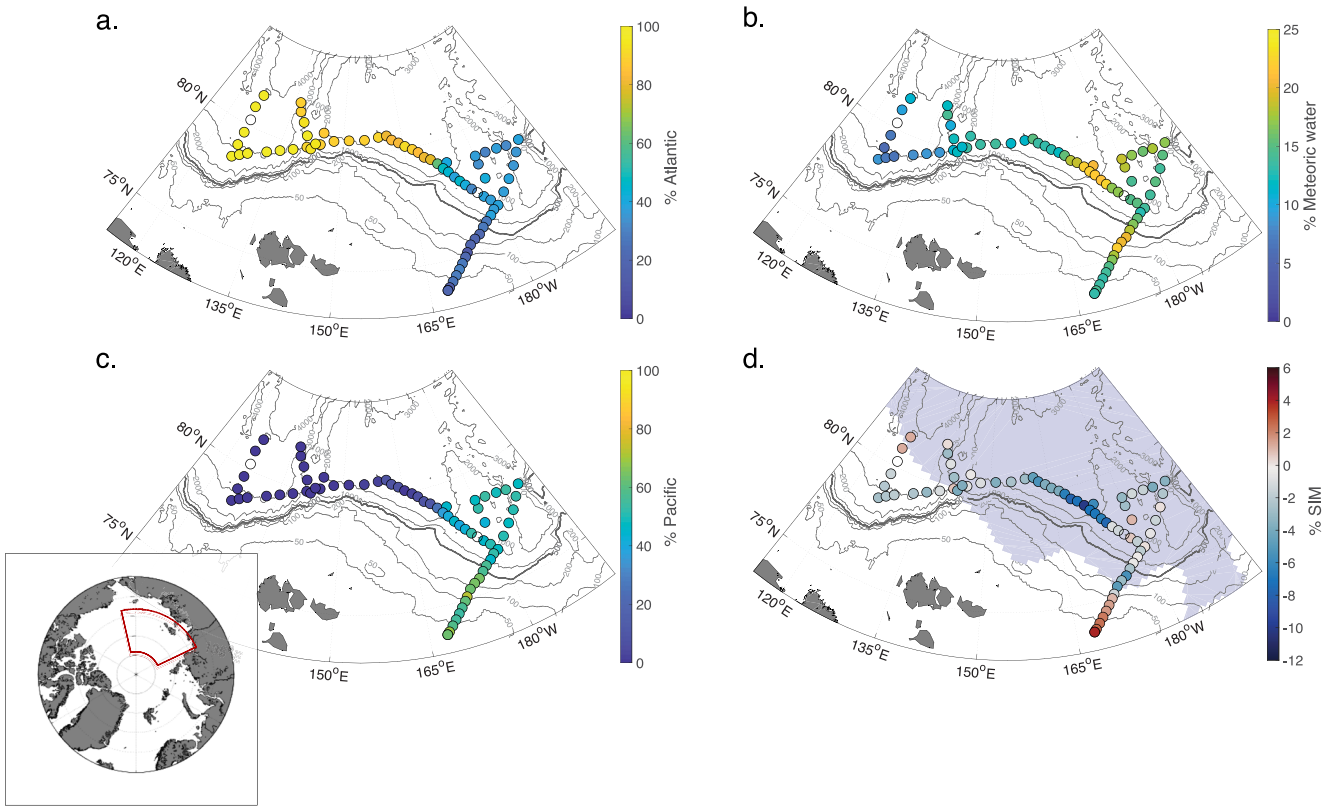

Figure 2. Percentage of (a) Atlantic-derived seawater, (b) meteoric water, (c) Pacific-derived seawater, and (d) sea ice melt in surface waters (2 m) on the 2021 transect. The 500 m isobath is shown in bold. Map inset shows the location of the study area outlined in red. Light purple shading on (d) indicates the monthly average sea ice extent for September 2021 (data from NSIDC, Fetterer et al., 2017).

3. Results

3.1. Water Mass Fractions

Atlantic- and Pacific-derived seawater were the principal water masses present in surface samples collected in 2021, with Atlantic-derived seawater dominant on the western half of the study area (extending to approximately 170°E) and Pacific-derived seawater dominant on the eastern half, particularly over the ESS (Figure 2). This is consistent with the source regions for these water masses; the Atlantic water enters the Arctic through Fram Strait and circulates cyclonically along the Barents and Kara shelves before reaching our study area, while the Pacific inflow enters through Bering Strait to the east of our study region and either veers west from the Chukchi Sea into the ESS or moves northward into the Makarov Basin. The largest percentages of meteoric water were observed along the East Siberian Slope near the Mendeleev Ridge (~170°E) and on the ESS transect. Negative percentages of sea ice melt (indicating ice & brine formation) were observed along the slope at the same locations as the high meteoric water percentages, and positive sea ice melt percentages were observed at the innermost stations along the ESS transect.

3.2. Radium-228

The ^{228}Ra activities measured in surface waters over the East Siberian Shelf and Slope in 2018 were 10.7–24.1 dpm/100 L (average of 17.1 ± 3.6 dpm/100 L, n = 18), with the highest activities over the shelf (water depth <500 m) and lower activities in the Makarov Basin (Figure 3a). In 2021, ^{228}Ra activities ranged from 1.3 to 40.8 dpm/100 L between 0 and 250 m, with activities increasing toward the east (Figures 3a, 4a, and 5a). Radium-228 levels in surface waters were highest (~25 dpm/100 L) on the slope near 170°E (stations 43–48), in the same area where high meteoric water percentages and negative sea ice melt percentages (i.e., high brine signatures) were observed, and along the ESS transect near the 200 m isobath (~20–30 dpm/100 L, near station 80), where salinity was slightly lower and meteoric water percentages were high.

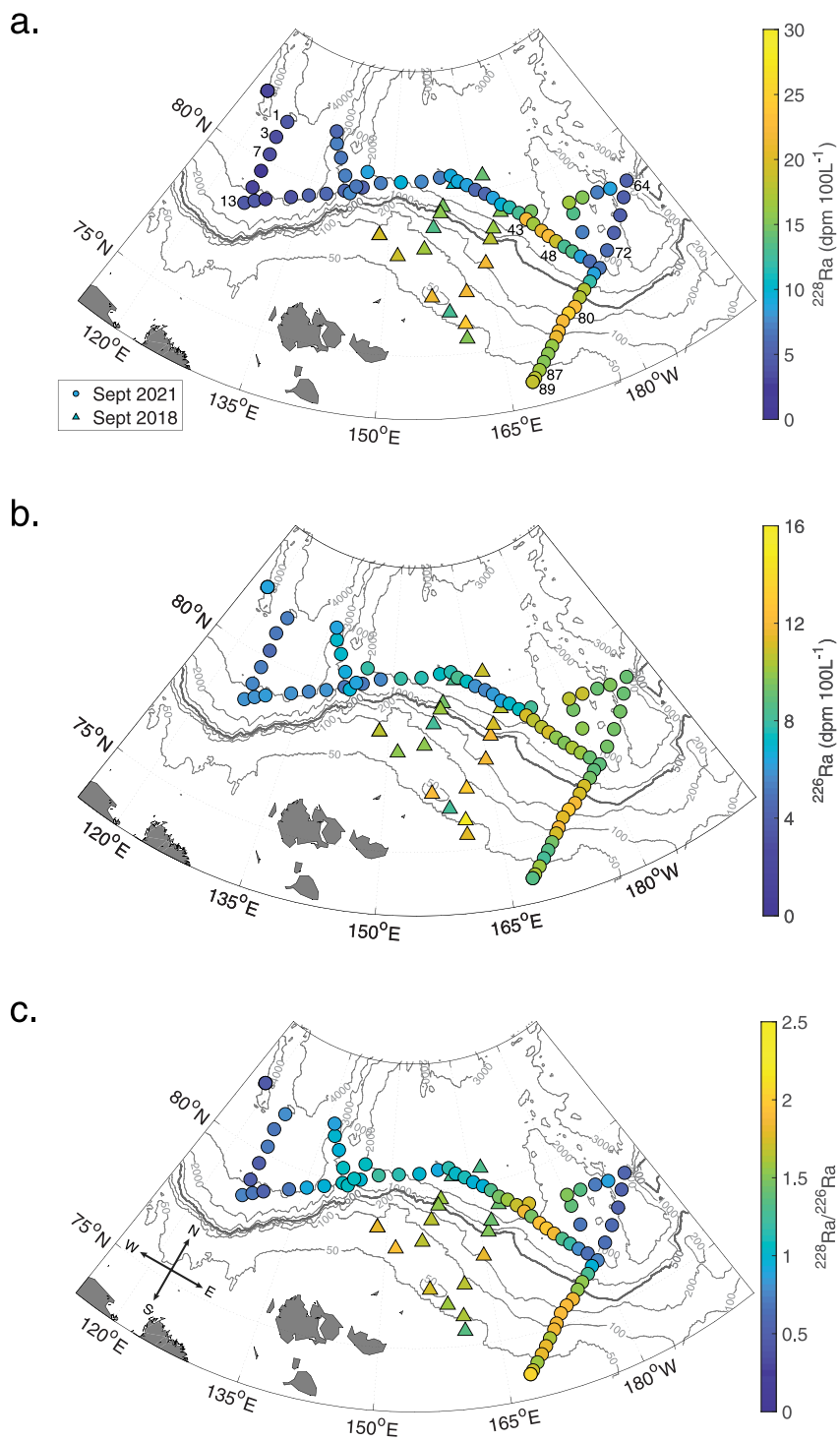

Figure 3. (a) Radium-228, (b) radium-226, and (c) the ^{228}Ra/^{226}Ra activity ratio in surface waters (2 m) on the Laptev and East Siberian Sea slopes in 2018 (triangles) and 2021 (circles). Higher radium levels over the shelf are consistent with a sedimentary source, and increased radium levels and activity ratios along the slope near 170°E in 2021 suggest the transport of shelf-influenced waters into the basin at this location. The 500 m isobath is shown in bold. 2021 stations mentioned in the text are labeled on panel (a).

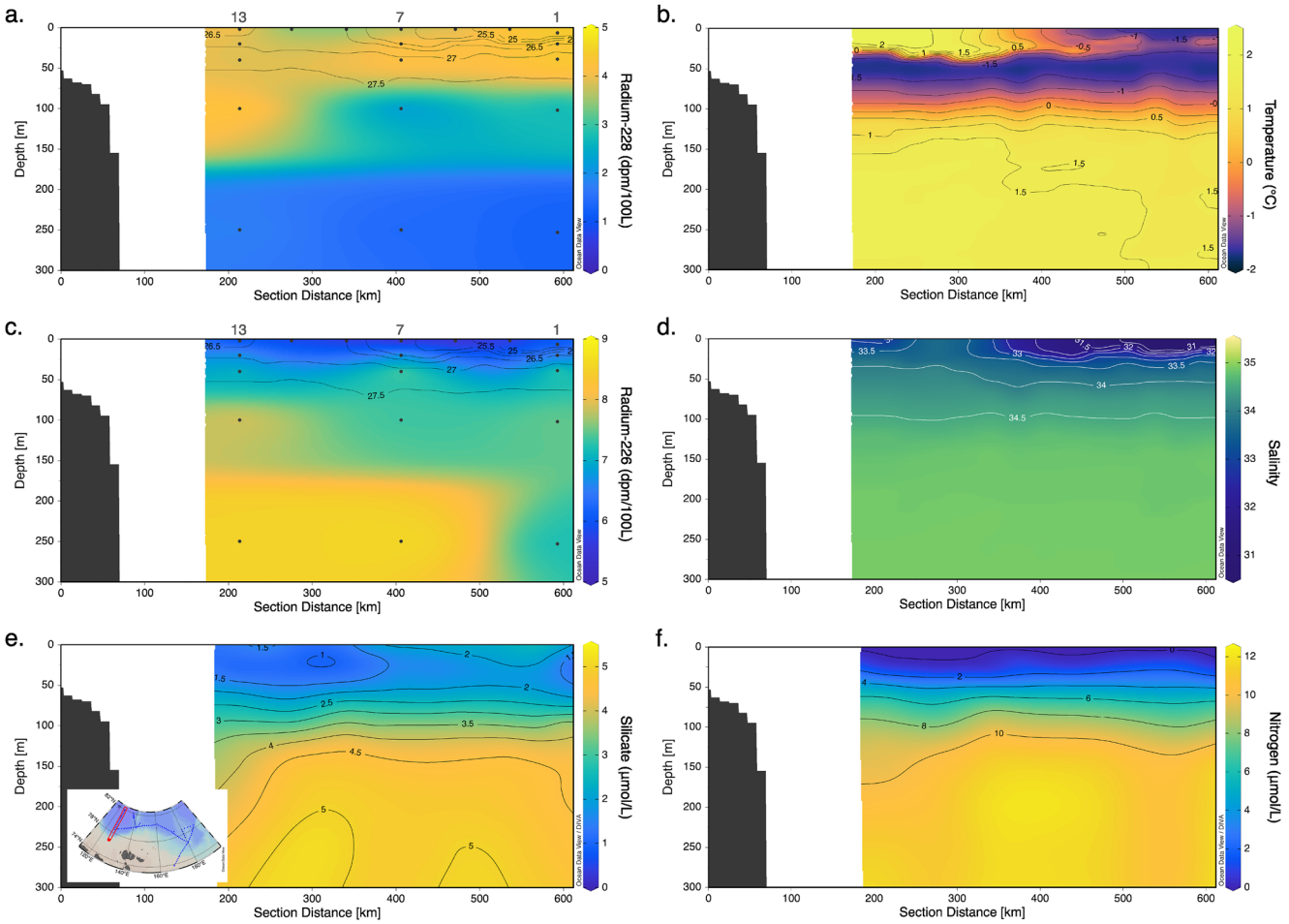

Figure 4. (a) Radium-228, (b) temperature, (c) radium-226, (d) salinity, (e) silicate, and (f) nitrogen (nitrate + nitrite) measured on the transect extending from the Laptev Sea slope into the Amundsen Basin. Radium-226 levels generally increase with depth while radium-228 is highest in surface waters, reflecting the strong shelf sediment source of this isotope. On the radium panels, sample collection depths are indicated with black dots, station numbers are labeled in gray on the top of each panel, and potential density contours (kg/m^3) overlay the radium distributions. The contours on the other panels are for their respective parameters and sample collection depths are not shown. Map inset on panel (e) shows the location of the transect in red. Figures were created using Ocean Data View (Schlitzer, 2023).

The highest ^{228}Ra activities were observed beneath the surface on the ESS transect. The maximum activity of 40.8 dpm/100 L was measured near the seafloor at one of the southernmost stations in the ESS (Station 87, 42 m), and activities between 11.9 and 40.8 dpm/100 L were observed on the shelf and slope (Figure 5a).

The offshore transects in the Amundsen Basin, including samples collected near the Lomonosov Ridge, had lower ^{228}Ra activities, increasing from 1.3 to 5.0 dpm/100 L in the Amundsen Basin to 1.7–9.3 dpm/100L near the Lomonosov Ridge. Activities around 4.6 dpm/100 L were observed in surface waters at Stations 1–3, in the central Amundsen Basin far from a shelf source (Figure 4a).

3.3. Radium-226

In 2018, ^{226}Ra activities were 8.1–15.0 dpm/100 L in surface waters (average = 10.7 ± 1.8 dpm/100 L, n = 18), with higher activities farther to the east (Figure 3b). The highest activity (15.0 dpm/100 L) was collected at the same location as the highest ^{228}Ra activity (24.1 dpm/100 L), at one of the southernmost stations along the 50 m isobath. In 2021, ^{226}Ra activities ranged from 4.6 to 18.0 dpm/100 L between 0 and 250 m, with activities generally increasing with depth and toward the east (Figures 3b, 4c, and 5c). At the surface, the ^{226}Ra distribution mirrors that of the Pacific water fraction (Figure 2c) and activities over the East Siberian Shelf and Slope (~9–13 dpm 100 L^{-1}) are similar to the ^{226}Ra values in the upper 1,000 m of the North Pacific (Chung & Craig, 1980; van Beek et al., 2022), reflecting the influence of Pacific water that has entered through Bering

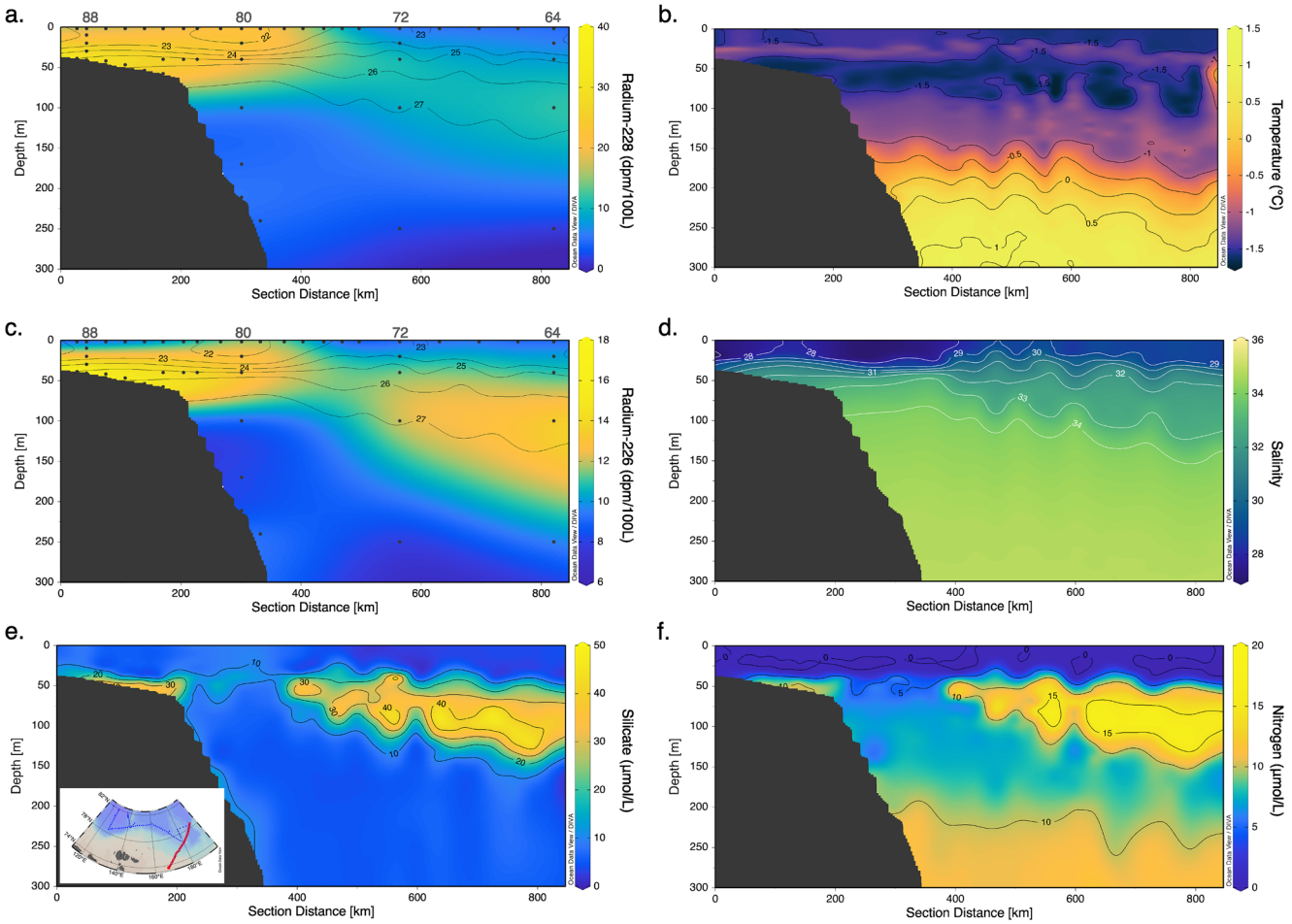

Figure 5. (a) Radium-228, (b) temperature, (c) radium-226, (d) salinity, (e) silicate, and (f) nitrogen (nitrate + nitrite) measured on the transect extending from the East Siberian Sea into the Makarov Basin. Radium levels are highest over the shelf, and the influence of Pacific-influenced halocline waters is evident in the radium-226 and nutrient distributions. On the radium panels, sample collection depths are indicated with black dots, station numbers are labeled in gray on the top of each panel, and potential density contours (kg/m^3) overlay the radium distributions. The contours on the other panels are for their respective parameters and sample collection depths are not shown. Map inset on panel (e) shows the location of the transect in red. Note difference in scale from Figure 4. Figures were created using Ocean Data View (Schlitzer, 2023).

Strait; some additional ^{226}Ra is likely added during transport west through the Chukchi and ESS. The highest surface water activities were measured along the East Siberian Slope near the 200 m isobath, in the same region where high ^{228}Ra activities, high meteoric water percentages, and negative sea ice melt percentages were observed (Figures 2 and 3).

Subsurface ^{226}Ra activities were highest near the seafloor on the ESS transect (18.0 dpm/100 L; Figure 5, Station 88, 41 m), reflecting the shelf source of this element. Increased ^{226}Ra activities (~13 dpm/100 L) are also apparent between 50 and 100 m on the basin end of the ESS transect (Figure 5c). In the Amundsen Basin, ^{226}Ra activities increase with depth with the exception of station 1. At this station, ^{226}Ra activities remain between 6.7 and 7.8 dpm/100 L between 20 and 250 m, while the other profiles on this transect (stations 7 and 13) increase up to 8.6 dpm/100 L (Figure 4c).

3.4. Radium-228/Radium-226 Ratios

In 2018, the ^{228}Ra/^{226}Ra activity ratios in the ESS were 1.3–2.0, with higher ratios being generally associated with lower salinities and higher fractions of meteoric water (Figure 3c). In 2021, ^{228}Ra/^{226}Ra activity ratios were 0.15–2.5. The highest ratios were found in the top 50 m and were either associated with high ^{228}Ra activities along the slope near 170°E (stations 43–48) or located over the shallow (<500 m) ESS. The maximum ^{228}Ra/^{226}Ra

ratio (2.5) was associated with the high Ra activities at station 87. Because ^{228}Ra is regenerated more quickly than ^{226}Ra in shelf sediments, a ratio >1 is typical of a shelf sediment porewater source of Ra; ratios as high as 3.9 have previously been observed in the Laptev Sea (Rutgers van der Loeff et al., 2003). Ratios were ∼1 in surface waters over the Lomonosov Ridge extending eastward to ∼165°E and were <1 in the Amundsen and Makarov Basins. Off the shelf, ratios generally decreased with depth. Lower ratios (<1) indicate that a longer time has elapsed since contact with the shelf, resulting in ^{228}Ra decay.

4. Discussion

4.1. ^{226}Ra Distribution in the Amundsen & Makarov Basins

In 2021, the surface water ^{228}Ra and ^{226}Ra activities at station 1, the northernmost station on the Amundsen Basin transect, were higher than those at station 13, the southernmost station on this transect (Figure 4). This increase in the center of the basin is opposite to the expected trend, given the shelf source of Ra. The higher Ra activities are associated with colder and fresher waters in the top ∼50 m (Figure 4), and with a high dissolved organic matter fluorescence (FDOM) signal (M. Papadimitraki, pers. comm.). Further, the ^{226}Ra activities do not increase with depth at this station, in contrast to the nutrient-type behavior that is characteristic of ^{226}Ra in most ocean basins. These results suggest the presence of a different water mass at this station compared to the other locations along the Amundsen Basin transect. This could be due to the presence of a mesoscale eddy, which may have transported slope waters (which are enriched in ^{228}Ra and FDOM, and freshened due to river discharge on the shelves) northward. Cold-core eddies associated with low salinity anomalies have been documented in the top 300 m of the Amundsen Basin and along the Laptev Slope (Pnyushkov et al., 2018) and Lomonosov Ridge (Woodgate et al., 2001). These eddies may initially form along the slope near Vilkitsky Trough, St. Anna Trough, and Fram Strait (Janout et al., 2015; Pnyushkov et al., 2018).

Radium-226 activities were higher in the Makarov Basin compared to the Amundsen Basin, with a local maximum between 50 and 100 m on the basin end of the ESS transect (Figure 5c). This increase is due to the presence of the Pacific-derived halocline in the Makarov Basin, which has high ^{226}Ra due to its Pacific origin and subsequent transport over the Chukchi Shelf (Kipp et al., 2019). The Pacific-derived halocline signal is also evidenced by elevated nutrient concentrations in this region (Figures 5e and 5f).

4.2. Surface Water Transport of Shelf-Derived Materials to the Central Arctic

The high Ra activities, ^{228}Ra/^{226}Ra activity ratios, meteoric water percentages, and sea ice brine percentages (negative sea ice melt percentages) associated with the samples collected along the slope near 170°E indicate that this is where shelf- and river-influenced waters are leaving the shelf and being transported into the central Arctic Ocean (Figures 2 and 3). This is likely the location where the TPD was leaving the shelf at the time of the 2021 expedition, though elevated ^{228}Ra activities, ^{228}Ra/^{226}Ra activity ratios, and meteoric water percentages extend westward to the Lomonosov Ridge, suggesting that there is also some transport of shelf-derived materials into the basin occurring along the length of the East Siberian Slope. The correlation between brine and meteoric water percentages is strongest in surface waters with low salinities (∼27–30); this likely indicates brine that was formed in coastal polynyas, where the strong river influence along the coast results in lower salinities (Bauch et al., 2011).

To estimate the residence time of surface waters on the shelf before crossing into the basin, we modeled the trajectories of water parcels in the top 10 m. Each model run includes 3 years of back-trajectories, indicating the path that each water parcel took over the shelves before entering the central Arctic along the East Siberian Slope (black line in Figure 6). The model was repeated three times, to cover the time period between 2012 and 2021. The time that each parcel spent in the ESS was very similar in the three model runs (mean of 2.4–2.6 months; Table 2). The time spent in the Laptev Sea was 6.7–7.2 months for the 2012–2015 and 2015–2018 time periods, and was slightly longer in 2018–2021 (10.8 ± 1.5 months) but not significantly different from the earlier years when the standard deviation is considered. These estimates are in line with previous evaluations of water residence times in the Laptev and East Siberian Seas: Bauch et al. (2009) estimate that the residence time of the bottom water in the Laptev Sea is at least one seasonal cycle, and Janout et al. (2020) determined the residence time of the Lena River plume to be on the order of a few months to >1 year.

The majority of the water parcels originate in the Laptev Sea, spending only a brief time in the outer ESS before crossing into the basin (Figure 6). The modeled trajectories are consistent with average surface water currents in July-September 2021 (based on the ORAS5 reanalysis product, see Section 2.5), which show the strongest

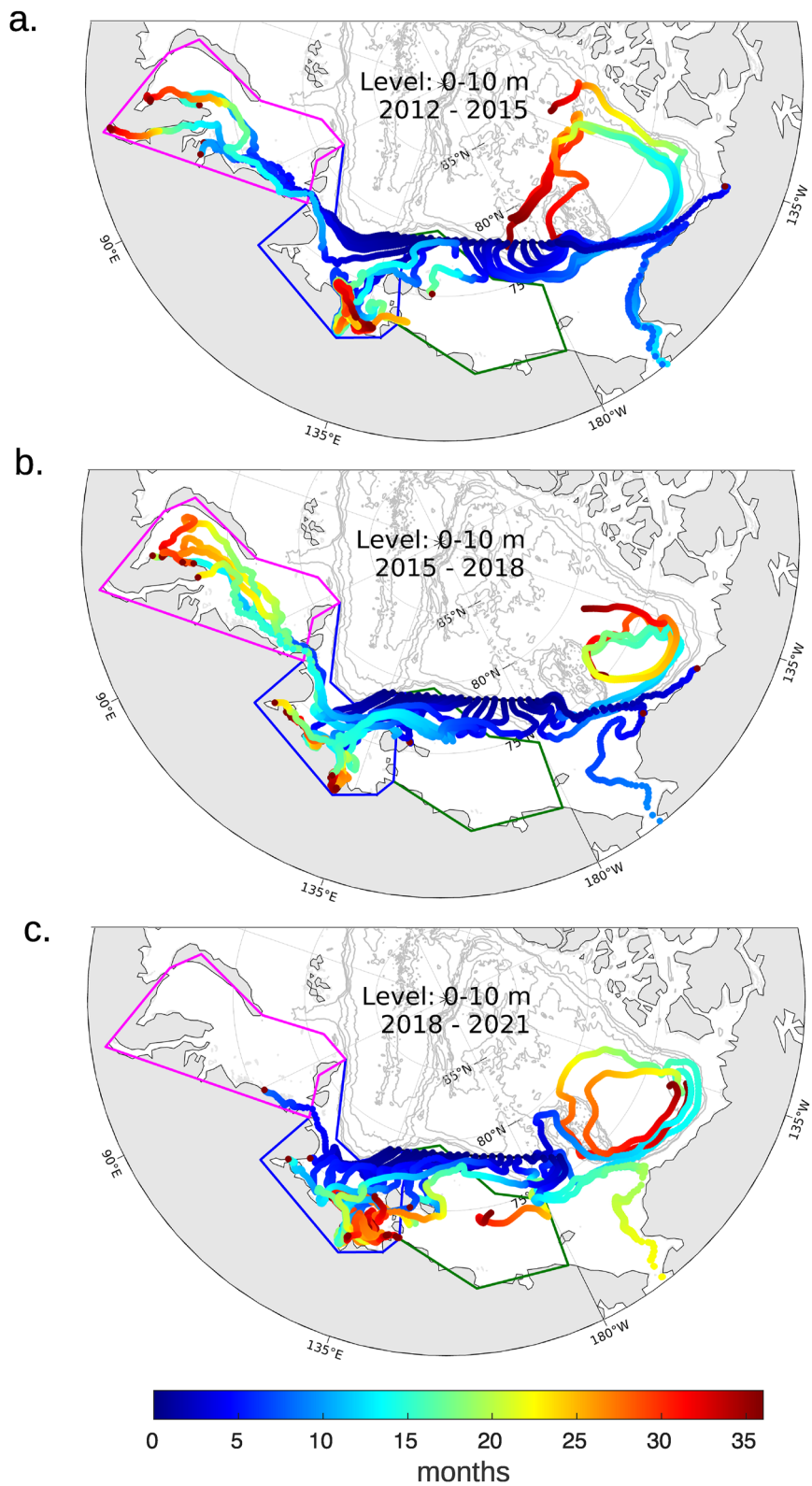

Figure 6. Average water parcel pathways prior to crossing the East Siberian shelf-basin boundary (black line) modeled for (a) 2012–2015, (b) 2015–2018, and (c) 2018–2021. Color indicates the time elapsed (in months) prior to crossing the boundary. The East Siberian, Laptev, and Kara Sea boundaries are outlined in green, blue, and pink, respectively. Most water parcels originated in the Laptev Sea and spent a brief time in the outer East Siberian Sea before crossing into the basin.

Table 2
Average Modeled Residence Times (in Months) of Surface Water Parcels (0–10 m) in Arctic Seas Before Crossing Into the Basin Along the East Siberian Slope (See Figure 6)

Time period	Residence time in East Siberian Sea (months)	Residence time in Laptev Sea (months)	Residence time in Kara Sea (months)
2012–2015	2.4 ± 1.0 (n = 8)	6.7 ± 2.1 (n = 10)	7.0 ± 2.4 (n = 6)
2015–2018	2.6 ± 0.4 (n = 13)	7.2 ± 1.3 (n = 15)	6.7 ± 0.8 (n = 7)
2018–2021	2.6 ± 0.8 (n = 15)	10.8 ± 1.5 (n = 15)	1.9 ± 0 (n = 1)

currents moving north/northeast above the New Siberian Islands and weaker currents recirculating water on the inner ESS rather than transporting it directly off the slope (Figure 7).

Here we consider the high-Ra waters near 170°E to represent the TPD signature in 2021. Based on the circulation model results (Figure 6), it is likely that the majority of this water originated in the Laptev Sea and that it spent a little over a year over the shelf before crossing the slope. Radium-228 activities around 20–25 dpm/100 L are consistent with this pathway along the outer ESS, as these activities are similar to those measured in surface waters northeast of the New Siberian Islands on the 2018 expedition (Figure 3).

The ^{228}Ra activities collected on the 2021 along-slope transect can be compared to previous measurements in the TPD to assess potential changes in the release of shelf-derived materials (Figure 8). The 2021 data set was collected much closer to the source of the TPD (the Laptev & East Siberian Seas) compared to previous years (2007–2015), which were collected in the central Arctic Ocean where the TPD travels along the Lomonosov Ridge (Figure 8a). However, the amount of radioactive decay that would have occurred during transport from the slope to the central Arctic (6%–11%, considering a 6–12 month transport time; Kipp et al., 2018) will not have a significant impact on the comparison.

The levels of ^{228}Ra observed in the TPD in the central Arctic Ocean in 2015 were higher than those observed in the TPD in 2007 or 2011 (Figure 8b), suggesting that there had been an increased flux of ^{228}Ra from Arctic shelves in the years preceding the 2015 sampling (Kipp et al., 2018; Rutgers van der Loeff et al., 2018). Plotting the ^{228}Ra activities as a function of the meteoric water percentages in each year rules out a change in the riverine source of radium as the driver of change, as the percentages are similar in each year. Further, a mass balance of ^{228}Ra sources presented in Kipp et al. (2018) shows that ~80% of the ^{228}Ra in Arctic surface waters is derived from the continental shelves, making changes in this source the most likely to be responsible for the observed increase. Because the TPD originates over the Laptev and East Siberian Shelves, changes in this area are likely to drive shifts in the chemistry of surface waters that are ultimately transported in the TPD. Kipp et al. (2018) hypothesized that an increased release of ^{228}Ra over the shelf may be driven by the loss of ice coverage over the shallow Laptev and ESS, which can facilitate stronger wind- and wave-driven mixing, thereby transporting ^{228}Ra

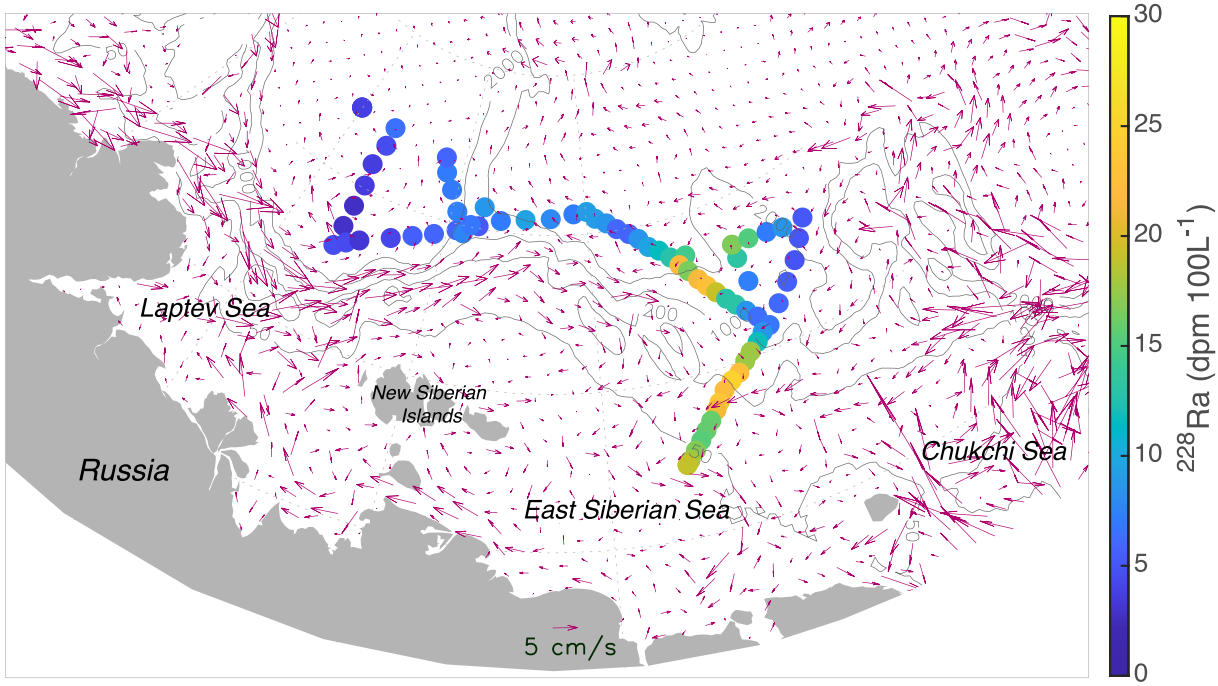

Figure 7. Average surface currents (red arrows) in the Laptev and East Siberian Seas for the period of July-September 2021. Radium-228 activities measured in September 2021 are shown beneath the currents (colored circles).

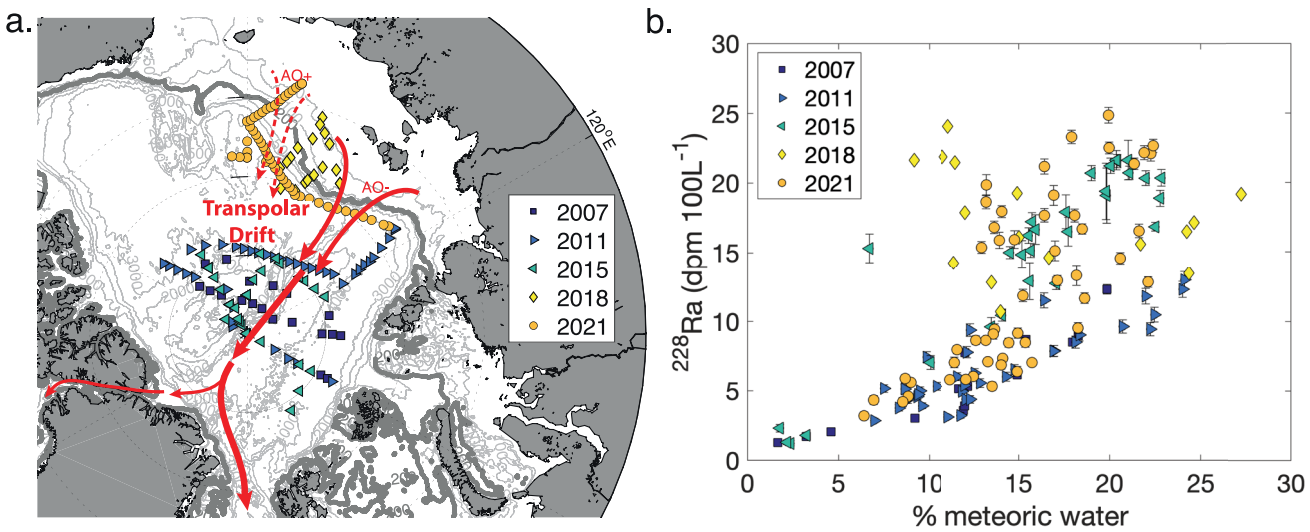

Figure 8. (a) Locations of radium samples collected in and around the path of the Transpolar Drift (TPD) between 2007 and 2021 and (b) surface water (up to 20 m) ^{228}Ra activities at these locations as a function of meteoric water percentage. Errors on the meteoric water percentage are 2% and are not shown. Samples collected between 2007 and 2015 are from Kipp et al. (2018) and Rutgers van der Loeff et al. (2018, 2012) and meteoric water fractions were recalculated using the method described in Section 2.4. Red arrows on panel (a) indicate the approximate pathway of the TPD under positive (dashed lines) and negative (solid lines) Arctic Oscillation states. Radium-228 activities increased in the TPD between 2007/2011 and 2015; the 2018 and 2021 activities measured on the Laptev and East Siberian Slopes are similar to the levels observed in 2015.

and other shelf-derived materials into the overlying water column. The weakening stratification of the halocline in the eastern Arctic may also contribute to increased shear-driven turbulent mixing in the summer months (Polyakov, Rippeth, Fer, Baumann, et al., 2020).

The ^{228}Ra activities measured near 170°E (associated with meteoric water >15%) are similar to those measured in the TPD in 2015. This supports the hypothesis that the chemistry of the TPD has been influenced by a larger input of shelf-derived elements over the last ~decade compared to the decade prior. However, the similarities between the 2015 and 2021 data sets suggest that the flux of shelf-derived materials has not increased further in recent years. Because these data sets were collected in different regions (Figure 8a), future sampling along the Laptev and East Siberian Slopes, as well as the construction of a seasonal time series to rule out changes due to sampling period, will help to further elucidate any trends in the flux of materials leaving these shelves (Kipp & Charette, 2022).

The current maps and water parcel trajectories presented here also highlight another possible source of variability in the ^{228}Ra levels in the TPD independent of sea ice changes: most of the water leaving the slope originates in the Laptev Sea, but the results of our 2021 expedition show that ^{228}Ra levels can be very high (>40 dpm/100 L) on the inner ESS. If more of the high-^{228}Ra water that is typically recirculating on the inner ESS becomes entrained into the water leaving the slope, this could increase the ^{228}Ra activities in the TPD.

4.3. Influence From the Lena River

Although rivers account for a much smaller percentage of Ra inputs to Arctic surface waters than continental shelves (~5% compared to 92% for ^{228}Ra; Bullock et al., 2022; Kipp et al., 2018), river discharge can nonetheless act as a significant source of Ra to Arctic seas. In 2021, elevated ^{228}Ra (21–25 dpm/100L) and ^{226}Ra (11–13 dpm/100L) activities were observed in the top 40 m along the East Siberian Slope near the 200 m isobath (stations 79–83; Figures 3, 5). These samples were also associated with lower salinities (~27–28) and higher meteoric water percentages (~20%), indicating the presence of river water. This is likely Lena River-influenced water that has been transported from the Laptev Sea. Although the Kolyma River empties directly into the ESS, its discharge and Ra activities are much lower than that of the Lena River, resulting in lower Ra fluxes (6×10^{12} vs. 52×10^{12} dpm ^{226}Ra/y and 6×10^{12} vs. 108×10^{12} dpm ^{228}Ra/y from the Kolyma and Lena, respectively; Bullock et al., 2022). The modeled water parcel back trajectories indicate water transport from the Laptev to the ESS

along the slope, supporting this hypothesis (Figure 6). The average July-September 2021 current directions similarly reflect transport along the slope, but also show some weaker transport in this area in the opposite direction, from the Chukchi Shelf (Figure 7). The influence of some Pacific-derived waters that had recently traveled over the Chukchi Shelf may also contribute to increased ^{228}Ra and ^{226}Ra activities.

4.4. Flux of ^{228}Ra From East Siberian & Laptev Shelf Sediments

The dominant feature of the ESS transect is the clear source of ^{228}Ra and ^{226}Ra from shelf sediments (Figure 5). To determine the magnitude of this ^{228}Ra source, a box model was constructed to represent the sources and sinks of ^{228}Ra in the Laptev and East Siberian Seas (Equation 1):

$$V \cdot \frac{\partial \mathrm{Ra}}{\partial t} = F_{\mathrm{sed}} \cdot A + F_{\mathrm{riv}} - \lambda \cdot [\mathrm{Ra_{shelf}}] \cdot V + [\mathrm{Ra_{inflow}}] \cdot V \cdot k - [\mathrm{Ra_{shelf}}] \cdot V \cdot k \quad (11)$$

In the above equation, V and A are the volume (m^3) and area (m^2) of the combined East Siberian and Laptev Seas, respectively, $\frac{\partial \mathrm{Ra}}{\partial t}$ is the change in the ^{228}Ra concentration through time (atoms m^{-3} d^{-1}), F_{sed} is the input of ^{228}Ra from shelf sediments (atoms m^{-2} d^{-1}), F_{riv} is the input of ^{228}Ra from rivers (atoms d^{-1}), λ is the ^{228}Ra decay constant (d^{-1}), [Ra_{shelf}] is the average ^{228}Ra concentration in the Laptev and ESS (atoms m^{-3}), [Ra_{inflow}] is the average ^{228}Ra concentration in water advected onto the shelf (atoms m^{-3}), and k is the inverse of the water residence time (d^{-1}). Sources of ^{228}Ra include inputs from shelf sediments, river discharge, and advection onto the shelf, while sinks include advection off the shelf and loss to decay.

We assume that the system is at steady-state (i.e., the concentration of ^{228}Ra is not changing through time) over the timescale of the average water residence time over the shelf (~9–13 months, see Section 4.2). Although there are likely climate-driven changes impacting the system over longer (annual-decadal) timescales (e.g., loss of sea ice, increased erosion), we assume that these will not have a significant impact on the ^{228}Ra inventory over seasonal timescales. Equation 1 can therefore be set equal to zero and solved for F_{sed} (Equation 2):

$$F_{\mathrm{sed}} = (([\mathrm{Ra_{shelf}}] - [\mathrm{Ra_{inflow}}]) \cdot h \cdot k) - (F_{\mathrm{riv}}/A) + (\lambda \cdot [\mathrm{Ra_{shelf}}] \cdot h) \quad (12)$$

where h is the average depth of the sea (in m). The Laptev and East Siberian Seas are considered together as one shelf sea in this model, because a combination of water from both shelves will contribute to the flux of shelf-derived elements that enters the TPD. The concentration of ^{232}Th, the parent isotope of ^{228}Ra, is similar in sediments on both shelves (Charkin et al., 2022). The surface area of the box extends from the coastline to the shelf break, defined by Jakobsson (2002) as 490 and 560 m for the Laptev and East Siberian Seas, respectively (bold contour line on Figures 1–3 indicates 500 m). The depth of the box (h) is equivalent to the average depth of the combined seas, 55 m (Jakobsson, 2002). [Ra_{inflow}] was estimated as the average ^{228}Ra concentration in waters flowing into the Laptev Sea via Vilkitsky Strait (data from Rutgers van der Loeff et al., 2003) and into the ESS via Bering Strait (data from Kipp et al., 2019): (3.67 ± 0.75) x 10^8 atoms/m^3. [Ra_{shelf}] is the average ^{228}Ra concentration measured in the top 60 m at stations with a bottom depth less than 500 m (such that they fall within the spatial boundaries of the shelf box): (9.28 ± 0.25) x10^8 atoms/m^3. To improve our spatial resolution, we include data from both the 2018 and 2021 expeditions in our estimate. However, the 2018 stations only have surface measurements, and both studies are located on the outer edge of the ESS; our average ^{228}Ra concentration may therefore be an underestimate because it is biased toward surface values (while we expect highest activities near the seafloor) and excludes the shallowest regions of the East Siberian and Laptev Seas. The ^{228}Ra source via river discharge into the Laptev and ESS is a total of 2.01 × 10^{18} atoms/d (Bullock et al., 2022). The average water residence time was estimated to be 13.4 ± 1.8 months, based on the modeled mean time water parcels spent over both shelves in 2018–2021 (see Section 4.2).

The resulting flux of ^{228}Ra from Laptev and ESS sediments is 9.03 × 10^7 atoms m^{-2} d^{-1}, with a possible range of 3.87 × 10^7–1.56 × 10^8 atoms m^{-2} d^{-1} based on the standard deviations in the average ^{228}Ra activities and the water residence time (Figure 9a). This value is similar to the flux of ^{228}Ra from the nearby Chukchi Shelf: Vieira et al. (2018) determined a flux of (1.49 ± 0.71) × 10^8 atoms m^{-2} d^{-1} in the spring when there was active water column overturning, and Kipp et al. (2020) estimated a flux of (1.70 ± 1.20) × 10^8 atoms m^{-2} d^{-1} over the southern Chukchi Shelf in the winter. The flux is higher than the average for all Arctic shelves (6.50 × 10^7 atoms m^{-2} d^{-1}, determined using the inventory of ^{228}Ra in Arctic surface waters and normalizing the shelf source to the overall shelf area; Kipp et al., 2018) and the global average ^{228}Ra flux from temperate regions (4.38 × 10^7 atoms

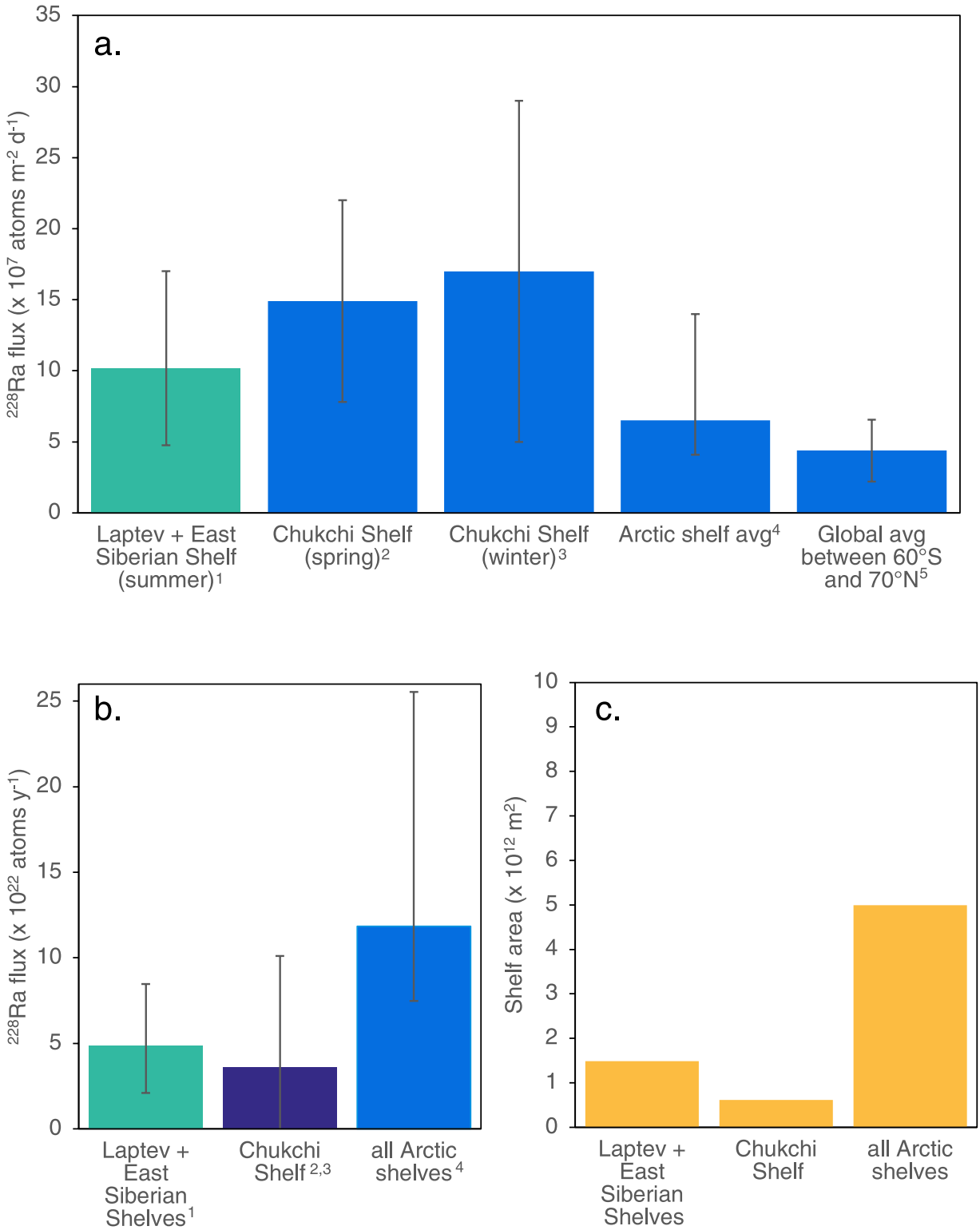

Figure 9. (a) The daily area-normalized ^{228}Ra flux from Arctic shelf sediments, (b) the annual ^{228}Ra flux from Arctic shelves, and (c) the area of Arctic shelves. The Laptev & East Siberian Shelves and the Chukchi Shelf contribute 41% and 30% of the pan-Arctic shelf ^{228}Ra flux while containing 30% and 12% of the pan-Arctic shelf area, respectively, indicating the importance of these shelves in influencing Arctic surface water chemistry. [1]This study; [2]Vieira et al. (2018); [3]Kipp et al. (2020); [4]Kipp et al. (2018); [5]Kwon et al. (2014). All shelf areas are from Jakobsson (2002).

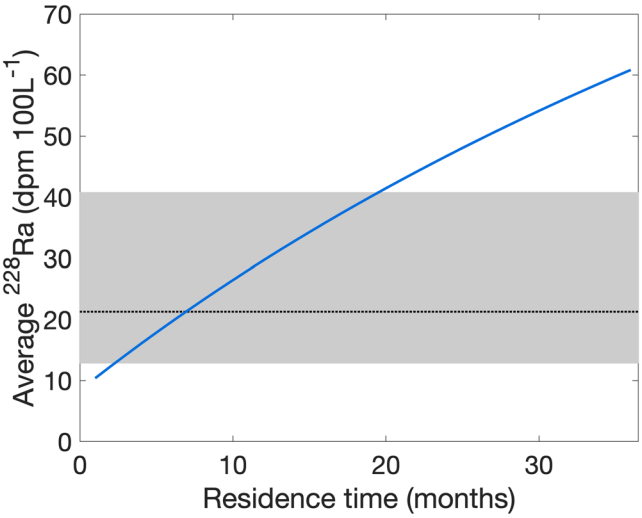

Figure 10. The average ^{228}Ra activity in the Laptev and East Siberian Seas (blue line) as a function of water residence time, using the box model presented in Section 4.4 and assuming the ^{228}Ra flux from sediments is equal to that on the Chukchi Shelf. The dashed black line denotes the average ^{228}Ra activity measured over the shelf on the 2021 expedition, and the gray shading indicates the range of observed activities. A water residence time of 3–20 months is required to accumulate the observed ^{228}Ra activities.

m^{-2} d^{-1}, determined using an inverse model; Kwon et al., 2014). This emphasizes the critical role that continental shelves play in modifying the chemistry of the Arctic Ocean, particularly compared to other ocean basins. Further, the East Siberian, Laptev, and Chukchi Shelves have a disproportionately large impact on sediment-derived element fluxes into Arctic surface waters.

The benthic ^{228}Ra flux was multiplied by shelf area to determine the annual ^{228}Ra flux from each shelf (Figures 9b and 9c). The Laptev and East Siberian flux (4.89×10^{22} atoms/y; this study) is higher than the Chukchi Shelf flux (3.61×10^{22} atoms/y; average of the area-normalized fluxes from Kipp et al., 2019; Vieira et al., 2018). These fluxes make up disproportionately high percentages of the pan-Arctic benthic ^{228}Ra flux (1.19×10^{23} atoms/y; Kipp et al., 2018); using this breakdown, the Laptev and ESS flux would together account for 41% of the total Arctic input of ^{228}Ra from sediments, with the Chukchi Shelf flux making up 30% of the total. These values are higher than expected based on shelf area, as the Laptev and East Siberian Shelves account for 30% of Arctic shelf area, while the Chukchi Shelf accounts for 12% of Arctic shelf area (Jakobsson, 2002). Thus, our analysis indicates that the Laptev, East Siberian, and Chukchi Shelves are contributing more ^{228}Ra (and presumably other sediment-derived elements) to Arctic surface waters than would be expected based on area alone. This may be due in part to the shallow depths of these shelves; they are the shallowest in the Arctic (~50–60 m), which may facilitate enhanced sediment-water column exchange via water column turbulence. The East Siberian and Laptev Seas are also experiencing rapid rates of sea ice decline due to increased upward heat flux resulting from the "atlantification" of the Eastern Arctic (Polyakov et al., 2017, 2020a), which may increase turbulence due to more wind and wave action on the open water. The large flux of sediment-derived materials coming from these shelves highlights the important role they play in controlling the chemistry of Arctic Ocean surface waters and the necessity of continuing to monitor changes in this sensitive region.

Our box model can also be used to provide an independent estimate of the water residence time over the shelf. Instead of solving for F_{sed}, if we assume that the flux of ^{228}Ra from sediments on the Laptev and ESS is the same as that on the Chukchi (1.60×10^8 atoms m^{-2} d^{-1}; Kipp et al., 2018; Vieira et al., 2018) we can solve Equation 12 for $[Ra]_{shelf}$ under different residence times and compare to the activities we observed on the ESS in 2021 (Figure 10). The longer the water spends over the shelf, the more Ra will accumulate. The range of ^{228}Ra activities observed in the ESS was 12.8–40.8 dpm/100 L, which requires a water residence time of 3–20 months. It takes 7 months to reach 21 dpm/100 L, the average observed ^{228}Ra activity. The residence time estimated from modeled current back-trajectories (13.4 ± 1.8 months) falls within this range. However, the residence time estimated from the current trajectories is focused on water parcels that are crossing the shelf-basin boundary, while the residence time estimate based on ^{228}Ra activities might be slightly longer because it reflects influence from water parcels that are recirculating over the ESS (where they can accumulate particularly high activities of ^{228}Ra).

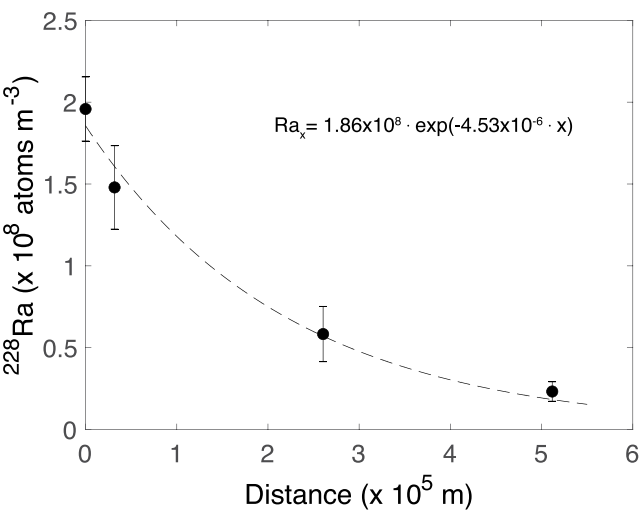

Figure 11. Excess ^{228}Ra activities between 200 and 250 m versus distance from the slope (station 80, ~211 m). With increasing distance from its slope sediment source, ^{228}Ra decreases due to horizontal eddy diffusion and radioactive decay. Black dashed line indicates the exponential line fit. The root mean square error of the line fit is 1.2×10^7 atoms m^{-3}.

4.5. Flux of ^{228}Ra From the Continental Slope

Similar to the pattern seen in shallower waters near the shelf break, ^{228}Ra activities in deeper waters (~250 m) decrease with distance from the continental slope (Figure 11). While the ^{228}Ra inputs from rivers and shallow shelf sediments may change seasonally, the ^{228}Ra flux from slope sediments should be relatively constant, allowing the assumption of a steady-state source. Once released from sediments, ^{228}Ra will decrease due to radioactive decay and transport off the slope by advection and diffusion. The upper Arctic Ocean

is highly stratified such that transport of ^{228}Ra and other margin-derived materials will occur horizontally along isopycnal surfaces (i.e., negligible vertical exchange). Advection in this area is generally along-slope (in the Arctic Circumpolar Boundary Current) rather than perpendicular to the shelf (Pnyushkov et al., 2021). The flux of ^{228}Ra should be consistent along the lengths of the Laptev and East Siberian slopes due to similar concentrations of its parent isotope, ^{232}Th (Charkin et al., 2022). Thus, the along-slope ^{228}Ra gradient is much lower than the cross-slope gradient, and advection along the slope in the Circumpolar Boundary Current should not affect the relationship between ^{228}Ra activity and distance from the slope. Assuming that on- and off-slope advection is not significant at this depth (~250 m), the decrease of ^{228}Ra with distance from the slope is controlled by horizontal eddy diffusion and radioactive decay following Equation 13 (Huh & Ku, 1998; Sanial et al., 2018):

$$\frac{\partial[\mathrm{Ra}]}{\partial t} = K_h \frac{\partial^2[\mathrm{Ra}]}{\partial x^2} - \lambda[\mathrm{Ra}] \tag{13}$$

where K_h is the apparent horizontal eddy diffusion coefficient (m^2/s), [Ra] is the ^{228}Ra concentration (atoms/m^3), x is the distance from the slope (m), and λ is the ^{228}Ra decay constant (3.82×10^{-9} s^{-1}). If on- or off-slope advection is significant, the impact of this process on the ^{228}Ra distribution would be captured in the K_h term, thus we designate this as an "apparent" horizontal eddy diffusion coefficient rather than a "true" horizontal eddy diffusion coefficient. There is evidence for off-slope currents on the order of 1–2 cm/s in this region (Pnyushkov et al., 2015), suggesting that the apparent horizontal eddy diffusivity we calculate here may overestimate the true horizontal eddy diffusivity. Nonetheless, it provides a useful estimate of the mixing timescales affecting radium isotopes and can be used to estimate the flux of ^{228}Ra from slope sediments as outlined below.

Assuming the concentration of ^{228}Ra reaches zero with infinite distance from the slope, Equation 13 can be rearranged into Equation 14:

$$[\mathrm{Ra}]_x = [\mathrm{Ra}]_0 e^{-xa} \tag{14}$$

Where Ra_0 and Ra_x are the concentrations of ^{228}Ra at the slope and at x meters from the slope, respectively, and a is the slope of the exponential line of best fit, equal to $\sqrt{\lambda/K_h}$. The ^{228}Ra activities measured between 200 and 250 m were used to determine the apparent horizontal eddy diffusion rate using Equation 14 (Figure 11). Because ^{228}Ra does not decrease to zero in the basin, the background open ocean ^{228}Ra activity was first subtracted from the measured ^{228}Ra activities to determine excess ^{228}Ra and meet the boundary condition that [Ra] decreases to zero. The background ^{228}Ra was estimated to be 1.0 dpm/100 L based on the average ^{228}Ra activities measured between 195–305 m over the Mendeleev Ridge and in the Makarov and Canada Basins on the 2015 GEOTRACES expedition (n = 6, 1.0 ± 0.4 dpm/100 L) (Kipp et al., 2018, 2019). Station 80 (depth ~211 m) was used as the start of the off-slope transect (x = 0).

The best estimate of K_h from the East Siberian slope is 186 m^2/s, with a possible range of 66–1,890 m^2/s based on the 95% confidence interval of the line fit (dashed black line on Figure 11). This value falls within the range of K_h values in the top 2,000 m of the water column compiled by Cole et al. (2015); the northern boundary of their study region was 60°N, where K_h values were estimated to be ~200 m^2/s based on Argo float measurements.

The flux of ^{228}Ra atoms from the slope (F_{slope}) can be calculated using Equation 15 (Sanial et al., 2018):

$$F_{\mathrm{slope}} = I \cdot \lambda \cdot \sin\theta \tag{15}$$

where I is the inventory of ^{228}Ra over the depth range of interest and θ represents the incline of the slope. Here we consider the slope between stations 82 (171.72°E, 74.95°N; 125 m) and 78 (176.14°E, 75.90°N; 417 m) (0.113°). The inventory of ^{228}Ra is estimated using the integral of Equation 14, where $[\mathrm{Ra}]_0/a = \mathrm{I}$. Using this approach, the best estimate of the ^{228}Ra inventory is 4.10×10^{13} atoms/m^3 (possible range of 1.88×10^{13}–1.60×10^{14} atoms/m^3) and the flux from the slope is 2.67×10^7 atoms m^{-2} d^{-1} (possible range of 1.23×10^7–1.04×10^8 atoms m^{-2} d^{-1}). This result is on the same order of magnitude as previous estimates of ^{228}Ra slope fluxes: Sanial et al. (2018) estimated a flux of 1.04×10^7 atoms m^{-2} d^{-1} from the Peruvian margin, and Hammond et al. (1990) reported fluxes of (1.43–2.89) $\times 10^7$ atoms m^{-2} d^{-1} in the Southern California Borderland.

5. Conclusions

Measurements of ^{228}Ra, ^{226}Ra, and water isotopes were combined with nutrient data and a model of water parcel trajectories to study the transfer of elements from the Laptev and East Siberian Seas into the central Arctic Ocean.

The largest signal of shelf- and river-influenced waters along the slope was located north of the ESS around 170°E, showing the likely location of the TPD at the time of sampling in September 2021. Modeled water parcel trajectories indicate that water spent ~13 months over the shelves before crossing the slope at this location. The ^{228}Ra levels in the TPD were similar to those observed in the central Arctic in 2015, which were notably higher than activities measured in previous years. This suggests that the flux of shelf-derived materials into the central Arctic has remained high but has not increased further.

The flux of radium-228 from the Laptev and East Siberian Slopes at 250 m is similar to estimates in other oceans, but the flux from shallow shelf sediments is higher than the average for temperate regions. Together, the Laptev, East Siberian, and Chukchi Shelves contribute a flux of shelf-derived materials to Arctic surface waters that is disproportionately high compared to their area. These shelves are therefore particularly important in controlling the chemistry of Arctic surface waters, and it is imperative that we continue to monitor this region for potential climate-driven changes. Future studies would benefit from increased sample resolution over the shelf and from the collection of sediment cores to calculate fluxes across the sediment-water interface; both of these measurements would help constrain the shelf sediment ^{228}Ra flux presented here.

Data Availability Statement

Data are available through the Arctic Data Center. Radium and water isotope data from 2021 and 2018 can be found at https://doi.org/10.18739/A2N58CN3B and https://doi.org/10.18739/A2FB4WN6B, respectively (Kipp & Charette, 2023a, 2023b). Nutrient data are available at https://doi.org/10.18739/A25T3G17R (Whitmore et al., 2023).

Acknowledgments
We thank the captains and crews of the *R/V Akademik Tryoshnikov* for coordinating two safe and successful sampling expeditions in 2018 and 2021. We appreciate the help of Rob Rember, who collected radium samples on the 2018 expedition, and the assistance of Adele Anderson and Jon Pazol, who were integral to the radium sampling effort on the 2021 expedition. We thank Paul Henderson for assistance with radium sample analysis and intercalibration efforts. This work was supported by National Science Foundation awards OPP-2031853 to L.E.K., OPP-2031854 to M.A.C, and OPP-1724523 to I.P and A.P.

References

Aagaard, K., & Carmack, E. C. (1989). The role of sea ice and other fresh water in the Arctic circulation. *Journal of Geophysical Research: Oceans*, *94*(C10), 14485–14498. https://doi.org/10.1029/jc094ic10p14485

Alkire, M. B., Morison, J., & Andersen, R. (2015). Variability in the meteoric water, sea-ice melt, and Pacific water contributions to the central Arctic Ocean, 2000-2014. *J. Geophys. Res. Ocean.*, *120*(3), 1573–1598. https://doi.org/10.1002/2014JC010023

Alkire, M. B., Rember, R., & Polyakov, I. V. (2019). Discrepancy in the identification of the Atlantic/Pacific front in the central Arctic Ocean: NO versus nutrient relationships. *Geophysical Research Letters*, *46*(7), 3843–3852. https://doi.org/10.1029/2018GL081837

Anderson, L. G., Björk, G., Holby, O., Jutterström, S., Magnus Mörth, C., O'Regan, M., et al. (2017). Shelf-Basin interaction along the East Siberian Sea. *Ocean Science*, *13*(2), 349–363. https://doi.org/10.5194/os-13-349-2017

Ardyna, M., Babin, M., Gosselin, M., Devred, E., Rainville, L., & Tremblay, J.-É. (2014). Recent Arctic Ocean sea ice loss triggers novel fall phytoplankton blooms. *Geophysical Research Letters*, *41*(17), 6207–6212. https://doi.org/10.1002/2014GL061047

Arrigo, K. R., van Dijken, G., & Pabi, S. (2008). Impact of a shrinking Arctic ice cover on marine primary production. *Geophysical Research Letters*, *35*(19). https://doi.org/10.1029/2008GL035028

Bauch, D., Dmitrenko, I., Kirillov, S., Wegner, C., Hölemann, J., Pivovarov, S., et al. (2009). Eurasian Arctic shelf hydrography: Exchange and residence time of southern Laptev Sea waters. *Continental Shelf Research*, *29*(15), 1815–1820. https://doi.org/10.1016/j.csr.2009.06.009

Bauch, D., Rutgersvan der Loeff, M., Andersen, N., Torres-Valdes, S., Bakker, K., & Abrahamsen, E. P. (2011). Physical oceanography, nutrients, and d^{18}O measured on water bottle samples during POLARSTERN cruise ARK-XXII/2. Suppl. to Bauch, D al. Orig. Freshw. polynya water Arct. Ocean halocline summer 2007. *Progress in Oceanography*, *91*(4), 482–495. https://doi.org/10.1594/PANGAEA.763451

Bolt, C. (2021). *Utility of trace element studies for improving our understanding of geochemical processes within the Arctic Ocean environment*. University of Alaska Fairbanks.

Brown, K. A., McLaughlin, F., Tortell, P. D., Yamamoto-Kawai, M., & Francois, R. (2016). Sources of dissolved inorganic carbon to the Canada Basin halocline: A multitracer study. *J. Geophys. Res. Ocean.*, *121*(5), 2918–2936. https://doi.org/10.1002/2015JC011535

Bullock, E. J., Kipp, L., Moore, W., Brown, K., Mann, P. J., Vonk, J. E., et al. (2022). Radium inputs into the Arctic Ocean from rivers: A basin-wide estimate. *J. Geophys. Res. Ocean.*, *127*(9). https://doi.org/10.1029/2022JC018964

Burt, W. J., Thomas, H., & Auclair, J.-P. (2013). Short-lived radium isotopes on the Scotian Shelf: Unique distribution and tracers of cross-shelf CO_2 and nutrient transport. *Marine Chemistry*, *156*, 120–129. https://doi.org/10.1016/j.marchem.2013.05.007

Charette, M. A., Kipp, L. E., Jensen, L. T., Dabrowski, J. S., Whitmore, L. M., Fitzsimmons, J. N., et al. (2020). The Transpolar Drift as a source of riverine and shelf-derived trace elements to the central Arctic Ocean. *Journal of Geophysical Research: Oceans*, *125*(5), e2019JC015920. https://doi.org/10.1029/2019JC015920

Charkin, A. N., Yaroshchuk, E. I., Dudarev, O. V., Leusov, A. E., Goriachev, V. A., Sobolev, I. S., et al. (2022). The influence of sedimentation regime on natural radionuclide activity concentration in marine sediments of the East Siberian Arctic Shelf. *Journal of Environmental Radioactivity*, *253–254*, 106988. https://doi.org/10.1016/j.jenvrad.2022.106988

Chung, Y., & Craig, H. (1980). ^{226}Ra in the Pacific Ocean. *Earth and Planetary Science Letters*, *49*(2), 267–292. https://doi.org/10.1016/0012-821X(80)90072-2

Chylek, P., Folland, C., Klett, J. D., Wang, M., Hengartner, N., Lesins, G., & Dubey, M. K. (2022). Annual mean Arctic amplification 1970–2020: Observed and simulated by CMIP6 climate models. *Geophysical Research Letters*, *49*(13). https://doi.org/10.1029/2022GL099371

Cole, S. T., Wortham, C., Kunze, E., & Owens, W. B. (2015). Eddy stirring and horizontal diffusivity from Argo float observations: Geographic and depth variability. *Geophysical Research Letters*, *42*(10), 3989–3997. https://doi.org/10.1002/2015GL063827

Dee, D. P., Uppala, S. M., Simmons, A. J., Berrisford, P., Poli, P., Kobayashi, S., et al. (2011). The ERA-interim reanalysis: Configuration and performance of the data assimilation system. *Quarterly Journal of the Royal Meteorological Society*, *137*(656), 553–597. https://doi.org/10.1002/qj.828

Devol, A. H., Codispoti, L. A., & Christensen, J. P. (1997). Summer and winter denitrification rates in western Arctic shelf sediments. *Continental Shelf Research*, *17*(9), 1029–1033. https://doi.org/10.1016/S0278-4343(97)00003-4

Dulaiova, H., Burnett, W. C., Wattayakorn, G., & Sojisuporn, P. (2006). Are groundwater inputs into river-dominated areas important? The Chao Phraya River - Gulf of Thailand. *Limnology & Oceanography*, *51*(5), 2232–2247. https://doi.org/10.4319/lo.2006.51.5.2232

Fetterer, F., Knowles, K., Meier, W. N., Savoie, M., & Windnagel, A. K. (2017). Sea Ice Index, version 3 [DataSet]. National Snow and Ice Data Center. https://doi.org/10.7265/N5K072F8

Günther, F., Overduin, P. P., Sandakov, A. V., Grosse, G., & Grigoriev, M. N. (2013). Short- and long-term thermo-erosion of ice-rich permafrost coasts in the Laptev Sea region. *Biogeosciences*, *10*(6), 4297–4318. https://doi.org/10.5194/bg-10-4297-2013

Hammond, D. E., Marton, R. A., Berelson, W. M., & Ku, T.-L. (1990). Radium 228 distribution and mixing in San Nicolas and San Pedro Basins, southern California Borderland. *Journal of Geophysical Research: Oceans*, *95*(C3), 3321–3335. https://doi.org/10.1029/JC095iC03p03321

Huh, C. A., & Ku, T. L. (1998). A 2-D section of ^{228}Ra and ^{226}Ra in the northeast Pacific. *Oceanologica Acta*, *21*(4), 533–542. https://doi.org/10.1016/S0399-1784(98)80036-4

Jakobsson, M. (2002). Hypsometry and volume of the Arctic Ocean and its constituent seas. *Geochemistry, Geophysics, Geosystems*, *3*(5), 1–18. https://doi.org/10.1029/2001GC000302

Janout, M. A., Aksenov, Y., Hölemann, J. A., Rabe, B., Schauer, U., Polyakov, I. V., et al. (2015). Kara Sea freshwater transport through Vilkitsky Strait: Variability, forcing, and further pathways toward the western Arctic Ocean from a model and observations. *J. Geophys. Res. Ocean.*, *120*(7), 4925–4944. https://doi.org/10.1002/2014JC010635

Janout, M. A., Hölemann, J., Laukert, G., Smirnov, A., Krumpen, T., Bauch, D., & Timokhov, L. (2020). On the variability of stratification in the freshwater-influenced Laptev Sea region. *Frontiers in Marine Science*, *7*. https://doi.org/10.3389/fmars.2020.543489

Jensen, L. T., Wyatt, N. J., Twining, B. S., Rauschenberg, S., Landing, W. M., Sherrell, R. M., & Fitzsimmons, J. N. (2019). Biogeochemical cycling of dissolved zinc in the western Arctic (Arctic GEOTRACES GN01). *Global Biogeochemical Cycles*, *33*(3), 343–369. https://doi.org/10.1029/2018GB005975

Jones, E. P., Anderson, L. G., Jutterström, S., Mintrop, L., & Swift, J. H. (2008). Pacific freshwater, river water and sea ice meltwater across Arctic Ocean basins: Results from the 2005 Beringia Expedition. *Journal of Geophysical Research: Oceans*, *113*(C8), C08012. https://doi.org/10.1029/2007JC004124

Jones, E. P., Anderson, L. G., & Swift, J. H. (1998). Distribution of Atlantic and Pacific waters in the upper Arctic Ocean: Implications for circulation. *Geophysical Research Letters*, *25*(6), 765–768. https://doi.org/10.1029/98GL00464

Kadko, D., Aguilar-Islas, A., Bolt, C., Buck, C. S., Fitzsimmons, J. N., Jensen, L. T., et al. (2019). The residence times of trace elements determined in the surface Arctic Ocean during the 2015 US Arctic GEOTRACES expedition. *Marine Chemistry*, *208*, 56–69. https://doi.org/10.1016/j.marchem.2018.10.011

Kelly, R. P., & Moran, S. B. (2002). Seasonal changes in groundwater input to a well-mixed estuary estimated using radium isotopes and implications for coastal nutrient budgets. *Limnology & Oceanography*, *47*(6), 1796–1807. https://doi.org/10.4319/lo.2002.47.6.1796

Kipp, L., & Charette, M. (2022). The Arctic Radium Isotope Observing Network (ARION): Tracking climate-driven changes in Arctic Ocean chemistry. *Oceanography*, *35*. https://doi.org/10.5670/oceanog.2022.105

Kipp, L., & Charette, M. (2023a). Arctic Radium Isotope Observing Network (ARION) 2021- radium, water isotopes, and salinity along Laptev & East Siberian Sea margins [Dataset]. Arctic Data Center. https://doi.org/10.18739/A2N58CN3B

Kipp, L., & Charette, M. (2023b). Radium, water isotopes, and salinity on the East Siberian Sea slope – NABOS 2018. [Dataset]. Arctic Data Center. https://doi.org/10.18739/A2FB4WN6B

Kipp, L. E., Charette, M. A., Moore, W. S., Henderson, P. B., & Rigor, I. G. (2018). Increased fluxes of shelf-derived materials to the central Arctic Ocean. *Science Advances*, *4*(1). https://doi.org/10.1126/sciadv.aao1302

Kipp, L. E., Kadko, D. C., Pickart, R. S., Henderson, P. B., Moore, W. S., & Charette, M. A. (2019). Shelf-Basin interactions and water mass residence times in the western Arctic Ocean: Insights provided by radium isotopes. *J. Geophys. Res. Ocean.*, *124*(5), 2019JC014988–3297. https://doi.org/10.1029/2019JC014988

Kipp, L. E., Spall, M. A., Pickart, R. S., Kadko, D. C., Moore, W. S., Dabrowski, J. S., & Charette, M. A. (2020). Observational and modeling evidence of seasonal trends in sediment-derived material inputs to the Chukchi Sea. *J. Geophys. Res. Ocean.*, *125*(5). https://doi.org/10.1029/2019JC016007

Klunder, M. B., Bauch, D., Laan, P., De Baar, H. J. W., Van Heuven, S., & Ober, S. (2012). Dissolved iron in the Arctic shelf seas and surface waters of the central Arctic Ocean: Impact of Arctic river water and ice-melt. *J. Geophys. Res. Ocean.*, *117*(C1). https://doi.org/10.1029/2011JC007133

Kwon, E. Y., Kim, G., Primeau, F., Moore, W. S., Cho, H.-M., DeVries, T., et al. (2014). Global estimate of submarine groundwater discharge based on an observationally constrained radium isotope model. *Geophysical Research Letters*, *41*(23), 8438–8444. https://doi.org/10.1002/2014GL061574

Letscher, R. T., Hansell, D. A., & Kadko, D. (2011). Rapid removal of terrigenous dissolved organic carbon over the Eurasian shelves of the Arctic Ocean. *Marine Chemistry*, *123*(1–4), 78–87. https://doi.org/10.1016/j.marchem.2010.10.002

Luo, D., Wu, Q., Jin, H., Marchenko, S. S., Lü, L., & Gao, S. (2016). Recent changes in the active layer thickness across the northern hemisphere. *Environmental Earth Sciences*, *75*(7), 555. https://doi.org/10.1007/s12665-015-5229-2

McClelland, J. W., Holmes, R. M., Dunton, K. H., & Macdonald, R. W. (2012). The Arctic Ocean Estuary. *Estuaries and Coasts*, *35*(2), 353–368. https://doi.org/10.1007/s12237-010-9357-3

Moody, A. (2022). *Evaluating the impact of submarine groundwater discharge on nutrients and trace elements in coastal systems: The examples of the Tuckean Swamp (Australia) and the Mississippi Sound (USA)*. University of Southern Mississippi.

Moore, W. S. (2006). The role of submarine groundwater discharge in coastal biogeochemistry. *Journal of Geochemical Exploration*, *88*(1–3), 389–393. https://doi.org/10.1016/j.gexplo.2005.08.082

Moore, W. S., & Dymond, J. (1991). Fluxes of ^{226}Ra and barium in the Pacific Ocean: The importance of boundary processes. *Earth and Planetary Science Letters*, *107*(1), 55–68. https://doi.org/10.1016/0012-821X(91)90043-H

Moore, W. S., & Reid, D. F. (1973). Extraction of radium from natural waters using manganese-impregnated acrylic fibers. *Journal of Geophysical Research*, *78*(36), 8880–8886. https://doi.org/10.1029/JC078i036p08880

Moore, W. S., & Todd, J. F. (1993). Radium isotopes in the Orinoco estuary and eastern Caribbean sea. *Journal of Geophysical Research: Oceans*, *98*(C2), 2233–2244. https://doi.org/10.1029/92JC02760

Nakayama, Y., Fujita, S., Kuma, K., & Shimada, K. (2011). Iron and humic-type fluorescent dissolved organic matter in the Chukchi Sea and Canada Basin of the western Arctic Ocean. *Journal of Geophysical Research: Oceans*, *116*(C7), 1–16. https://doi.org/10.1029/2010JC006779

Newton, R., Schlosser, P., Mortlock, R., Swift, J., & MacDonald, R. (2013). Canadian Basin freshwater sources and changes: Results from the 2005 Arctic Ocean Section. *Journal of Geophysical Research: Oceans*, *118*(4), 2133–2154. https://doi.org/10.1002/jgrc.20101

Peterson, B. J., Holmes, R. M., McClelland, J. W., Vörösmarty, C. J., Lammers, R. B., Shiklomanov, A. I., et al. (2002). Increasing river discharge to the Arctic Ocean. *Science*, *298*(5601), 2171–2173. https://doi.org/10.1126/science.1077445

Peterson, R. N., Burnett, W. C., Taniguchi, M., Chen, J., Santos, I. R., & Misra, S. (2008). Determination of transport rates in the Yellow River–Bohai Sea mixing zone via natural geochemical tracers. *Continental Shelf Research*, *28*(19), 2700–2707. https://doi.org/10.1016/j.csr.2008.09.002

Pnyushkov, A., Polyakov, I. V., Padman, L., & Nguyen, A. T. (2018). Structure and dynamics of mesoscale eddies over the Laptev Sea continental slope in the Arctic Ocean. *Ocean Science*, *14*(5), 1329–1347. https://doi.org/10.5194/os-14-1329-2018

Pnyushkov, A. V., Polyakov, I. V., Alekseev, G. V., Ashik, I. M., Baumann, T. M., Carmack, E. C., et al. (2021). A steady regime of volume and heat transports in the eastern Arctic Ocean in the early 21st century. *Frontiers in Marine Science*, *8*, 1–13. https://doi.org/10.3389/fmars.2021.705608

Pnyushkov, A. V., Polyakov, I. V., Ivanov, V. V., Aksenov, Y., Coward, A. C., Janout, M., & Rabe, B. (2015). Structure and variability of the boundary current in the Eurasian Basin of the Arctic Ocean. *Deep Sea Research Part I: Oceanography Research Papers*, *101*, 80–97. https://doi.org/10.1016/j.dsr.2015.03.001

Polyakov, I. V., Ingvaldsen, R. B., Pnyushkov, A. V., Bhatt, U. S., Francis, J. A., Janout, M., et al. (2023). Fluctuating Atlantic inflows modulate Arctic atlantification. *Science*, *381*(6661), 972–979. https://doi.org/10.1126/science.adh5158

Polyakov, I. V., Pnyushkov, A. V., Alkire, M. B., Ashik, I. M., Baumann, T. M., Carmack, E. C., et al. (2017). Greater role for Atlantic inflows on sea-ice loss in the Eurasian Basin of the Arctic Ocean. *Science*, *356*(6335), 285–291. https://doi.org/10.1126/science.aai8204

Polyakov, I. V., Rippeth, T. P., Fer, I., Alkire, M. B., Baumann, T. M., Carmack, E. C., et al. (2020). Weakening of cold halocline layer exposes sea ice to oceanic heat in the Eastern Arctic Ocean. *Journal of Climate*, *33*(18), 8107–8123. https://doi.org/10.1175/JCLI-D-19-0976.1

Polyakov, I. V., Rippeth, T. P., Fer, I., Baumann, T. M., Carmack, E. C., Ivanov, V. V., et al. (2020). Intensification of near-surface currents and shear in the Eastern Arctic Ocean. *Geophysical Research Letters*, *47*(16). https://doi.org/10.1029/2020GL089469

Rainville, L., & Woodgate, R. A. (2009). Observations of internal wave generation in the seasonally ice-free Arctic. *Geophysical Research Letters*, *36*(23), L23604. https://doi.org/10.1029/2009GL041291

Rantanen, M., Karpechko, A. Y., Lipponen, A., Nordling, K., Hyvärinen, O., Ruosteenoja, K., et al. (2022). The Arctic has warmed nearly four times faster than the globe since 1979. *Communications Earth & Environment*, *3*(1), 168. https://doi.org/10.1038/s43247-022-00498-3

Rawlins, M. A., Steele, M., Holland, M. M., Adam, J. C., Cherry, J. E., Francis, J. A., et al. (2010). Analysis of the Arctic system for freshwater cycle intensification: Observations and expectations. *Journal of Climate*, *23*(21), 5715–5737. https://doi.org/10.1175/2010JCLI3421.1

Reid, D. F. (1984). Radium variability produced by shelf-water transport and mixing in the western Gulf of Mexico. *Deep-Sea Research*, *31*(12), 1501–1510. https://doi.org/10.1016/0198-0149(84)90084-0

Rodellas, V., Garcia-Orellana, J., Trezzi, G., Masqué, P., Stieglitz, T. C., Bokuniewicz, H., et al. (2017). Using the radium quartet to quantify submarine groundwater discharge and porewater exchange. *Geochimica et Cosmochimica Acta*, *196*, 58–73. https://doi.org/10.1016/j.gca.2016.09.016

Rutgers van der Loeff, M., Cai, P., Stimac, I., Bauch, D., Hanfland, C., Roeske, T., & Moran, S. B. (2012). Shelf-basin exchange times of Arctic surface waters estimated from ^{228}Th/^{228}Ra disequilibrium. *Journal of Geophysical Research: Oceans*, *117*(C3), C03024. https://doi.org/10.1029/2011JC007478

Rutgers van der Loeff, M., Kipp, L. E., Charette, M. A., Moore, W. S., Black, E., Stimac, I., et al. (2018). Radium isotopes across the Arctic Ocean show time scales of water mass ventilation and increasing shelf inputs. *Journal of Geophysical Research: Oceans*, *123*(7), 4853–4873. https://doi.org/10.1029/2018JC013888

Rutgers van der Loeff, M., Kuhne, S., Wahsner, M., Holtzen, H., Frank, M., Ekwurzel, B., et al. (2003). ^{228}Ra and ^{226}Ra in the Kara and Laptev seas. *Continental Shelf Research*, *23*(1), 113–124. https://doi.org/10.1016/S0304-4203(98)00070-X

Sanial, V., Kipp, L. E., Henderson, P. B., van Beek, P., Reyss, J.-L., Hammond, D. E., et al. (2018). Radium-228 as a tracer of dissolved trace element inputs from the Peruvian continental margin. *Marine Chemistry*, *201*, 20–34. https://doi.org/10.1016/j.marchem.2017.05.008

Schlitzer, R. (2023). *Ocean data view*. odv.awi.de.

Schulz, K., Büttner, S., Rogge, A., Janout, M., Hölemann, J., & Rippeth, T. P. (2021). Turbulent mixing and the formation of an intermediate nepheloid layer above the Siberian continental shelf break. *Geophysical Research Letters*, *48*(9). https://doi.org/10.1029/2021GL092988

Schulz, K., Lincoln, B., Povazhnyy, V., Rippeth, T., Lenn, Y.-D., Janout, M., et al. (2022). Increasing nutrient fluxes and mixing regime changes in the eastern Arctic Ocean. *Geophysical Research Letters*, *49*(5). https://doi.org/10.1029/2021GL096152

van Beek, P., François, R., Conte, M., Reyss, J. L., Souhaut, M., & Charette, M. (2007). ^{228}Ra/^{226}Ra and ^{226}Ra/Ba ratios to track barite formation and transport in the water column. *Geochimica et Cosmochimica Acta*, *71*(1), 71–86. https://doi.org/10.1016/j.gca.2006.07.041

van Beek, P., François, R., Honda, M., Charette, M. A., Reyss, J. L., Ganeshram, R., et al. (2022). Fractionation of ^{226}Ra and Ba in the upper North Pacific Ocean. *Frontiers in Marine Science*, *9*. https://doi.org/10.3389/fmars.2022.859117

Vieira, L. H., Achterberg, E. P., Scholten, J., Beck, A. J., Liebetrau, V., Mills, M. M., & Arrigo, K. R. (2018). Benthic fluxes of trace metals in the Chukchi Sea and their transport into the Arctic Ocean. *Marine Chemistry*, *208*, 43–55. https://doi.org/10.1016/j.marchem.2018.11.001

Wheeler, P. A., Watkins, J. M., & Hansing, R. L. (1997). Nutrients, organic carbon and organic nitrogen in the upper water column of the Arctic Ocean: Implications for the sources of dissolved organic carbon. *Deep Sea Research Part II: Topical Studies in Oceanography*, *44*(8), 1571–1592. https://doi.org/10.1016/S0967-0645(97)00051-9

Whitmore, L. M., Kaufman, M., Pnuyshkov, A., & Polyakov, I. (2023). Nansen and Amundsen Basins Observational System II (NABOS II) – Seawater macronutrient observations in the eastern Eurasian and Makarov Basins, Arctic Ocean, 2021 [Dataset]. Arctic Data Center. https://doi.org/10.18739/A25T3G17R

Whitmore, L. M., Pasqualini, A., Newton, R., & Shiller, A. M. (2020). Gallium: A new tracer of Pacific water in the Arctic Ocean. *Journal of Geophysical Research: Oceans*, *125*(7). https://doi.org/10.1029/2019JC015842

Woodgate, R. A., Aagaard, K., Muench, R. D., Gunn, J., Björk, G., Rudels, B., et al. (2001). The Arctic Ocean boundary current along the Eurasian slope and the adjacent Lomonosov ridge: Water mass properties, transports and transformations from moored instruments. *Deep Sea Research Part I: Oceanography Research Papers*, *48*(8), 1757–1792. https://doi.org/10.1016/S0967-0637(00)00091-1

Yamamoto-Kawai, M., McLaughlin, F. A., Carmack, E. C., Nishino, S., & Shimada, K. (2008). Freshwater budget of the Canada Basin, Arctic Ocean, from salinity, δ^{18}O, and nutrients. *Journal of Geophysics Research: Ocean*, *113*(C1). https://doi.org/10.1029/2006JC003858

Zuo, H., Balmaseda, M. A., Tietsche, S., Mogensen, K., & Mayer, M. (2019). The ECMWF operational ensemble reanalysis-analysis system for ocean and sea ice: A description of the system and assessment. *Ocean Science*, *15*(3), 779–808. https://doi.org/10.5194/os-15-779-2019